



# AMERICAN METEOROLOGICAL SOCIETY

*Journal of Climate*

## EARLY ONLINE RELEASE

This is a preliminary PDF of the author-produced manuscript that has been peer-reviewed and accepted for publication. Since it is being posted so soon after acceptance, it has not yet been copyedited, formatted, or processed by AMS Publications. This preliminary version of the manuscript may be downloaded, distributed, and cited, but please be aware that there will be visual differences and possibly some content differences between this version and the final published version.

The DOI for this manuscript is doi: 10.1175/2008JCLI2827.1

The final published version of this manuscript will replace the preliminary version at the above DOI once it is available.



# Projected changes to the Southern Hemisphere ocean and sea-ice in the IPCC AR4 climate models

Alexander Sen Gupta

Agus Santoso

Andréa S. Taschetto

Caroline C. Ummenhofer

Matthew H. England

Jessica Trevena

Climate Change Research Centre (CCRC), Faculty of Science, University of New South Wales, Sydney, NSW, Australia.

For: Journal of Climate

Correspondence Author: Alex Sen Gupta, [a.sengupta@unsw.edu.au](mailto:a.sengupta@unsw.edu.au)

Climate Change Research Centre (CCRC), Faculty of Science, University of New South Wales, Sydney, NSW, Australia

**Abstract.** Fidelity and projected changes in the climate models, used for the Intergovernmental Panel on Climate Change (IPCC) Fourth Assessment Report (AR4), are assessed with regard to the Southern Hemisphere extratropical ocean and sea-ice systems. While individual models span different physical parameterisations and resolutions, a major component of inter-model variability results from surface wind differences. Projected changes to the surface wind-field is also central in modifying future extratropical circulation and internal properties. A robust southward shift of the circumpolar current and subtropical gyres is projected, with a strong spin-up of the Atlantic gyre. An associated increase in the core strength of the circumpolar circulation is evident; however, this does not translate into robust increases in Drake Passage transport. While an overarching oceanic warming is projected, the circulation-driven poleward shift of the temperature field explains much of the midlatitude warming pattern. The effect of this shift is less clear for salinity, where instead, surface freshwater forcing dominates. Surface warming and high-latitude freshwater increases drive intensified stratification, and a shoaling and southward shift of the deep mixed layers. Despite large inter-model differences, there is also a robust weakening in bottom water formation and its northward outflow. At the same time the wind intensification invigorates the upwelling of deep water, transporting warm, salty water southwards and upwards, with major implications for sequestration and outgassing of CO<sub>2</sub>. A robust decrease is projected for both the sea-ice concentration and the seasonal cycling of ice volume, potentially altering the salt and heat budget at high-latitudes.

## 1. Introduction

The Southern Ocean acts as the engine room to the world's overturning circulation drawing its energy from the powerful mid-latitude westerlies acting over a zonally continuous ocean. A high-latitude wind-driven divergence draws deep waters to the surface. Subsequently these upwelled waters are driven both north and south via Ekman fluxes and buoyancy driven sinking around the Antarctic margin. The northwards flow subducts to form the basis of the thermocline, mode and intermediate water masses that comprise the upper limb of the global overturning circulation. The southwards flow, modified by a salt injection from sea-ice development and large winter heat losses, forms the densest bottom water-masses that ventilate the abyssal ocean. These vertical movements of water help to set the density structure of the Southern Ocean.

Intimately linked to this overturning circulation is the zonally continuous Antarctic Circumpolar Current (ACC) that connects the three ocean basins with a transport of  $\sim 135\text{Sv}$  through the Drake Passage (e.g. Cunningham *et al.*, 2003). Surface wind and buoyancy forcing, internal circulation, the underlying bathymetry and the action of mesoscale eddies all play a role in determining its characteristics (Gent *et al.*, 2001; Rintoul *et al.*, 2001; Olbers *et al.*, 2004). At lower latitudes, gradients in the surface wind-stress, largely determine the dynamics of the subtropical gyres that control the flow pathways that extend from the surface down to intermediate depths. The Southern Ocean also hosts the most expansive volume of homogeneous mode waters, formed through vigorous winter convection. Annual communication between the surface and ocean interior mean that this water-mass sequesters large quantities of heat and gases from the atmosphere. This is complemented by the formation and northward export of Antarctic Intermediate Water (AAIW) into the ocean mid-depths and Antarctic Bottom Water (AABW) into the abyssal ocean. Observational studies have shown that these water masses play a major role in the removal of additional anthropogenic  $\text{CO}_2$  (Sabine *et al.*, 2004) and heat (Gille, 2002;



IPCC, 2007) and that furthermore, the properties of these water-masses have been subject to significant trends over recent decades (e.g., Bindoff and McDougall, 2000; Bryden *et al.*, 2003; Aoki *et al.*, 2005a,b; Johnson *et al.*, 2007; Rintoul, 2007).

The Southern Hemisphere (SH) boasts one of the most profound and robust climate trends observed over the past few decades - characterised by a poleward shift and strengthening of the mid-latitude jet (Kushner *et al.*, 2001) and more generally of the mid-latitude westerly winds. This is often described in terms of a shift to an increasingly positive phase of the dominant mode of extratropical variability, the Southern Annular Mode (SAM; e.g., Thompson *et al.*, 2000; Thompson and Solomon, 2002; Marshall *et al.*, 2004). This trend has been linked to changes in both stratospheric ozone and greenhouse forcing (Gillett and Thompson, 2003; Thompson and Solomon, 2002). Moreover, the surface signature of this atmospheric rearrangement has the potential to significantly modify characteristics of the ocean and sea-ice systems (Hall and Visbeck, 2002; Sen Gupta and England, 2006). This modification of the general circulation is on the backdrop of, and intimately tied to, unprecedented, large-scale increases in global temperatures and modifications to the hydrological cycle (IPCC, 2007).

In light of both the observed and projected changes to the surface forcing there has been a growing focus on the Southern Ocean, driven in part by a recognition of the potential changes to its enormous sequestration capacity. This has profound consequences when considering requirements for the mitigation of future climate change (e.g., Russell *et al.*, 2006a; Toggweiler and Russell, 2008; Friedlingstein, 2008). Scientific progress has been greatly aided by the availability of model output from the Coupled Model Intercomparison Project (CMIP3), used as part of the Intergovernmental Panel on Climate Change (IPCC) Fourth Assessment Report (AR4), that covers a wide range of control and forced scenarios. Most of the AR4 models show robust changes in the SH mid-latitude westerlies over the 20th century, however, the poleward intensification tends to be underestimated compared to

recent observations (Yin, 2005). Furthermore, Fyfe and Saenko (2006) show that for a subset of the AR4 models this projected trend continues under increasing greenhouse forcing.

In model experiments using both an ocean only model (Oke and England, 2004) and an intermediate complexity climate model (Fyfe *et al.*, 2007), changes in the position and strength of the mid-latitude westerlies are shown to induce major changes in Southern Ocean temperature extending from the surface to intermediate depths, independent of any surface warming. As such, one might expect an associated modification of the circulation into the future. Such shifts were found by Fyfe and Saenko (2006) in the Southern Ocean across a subset of CMIP3 models, with a poleward contraction and strengthening of the zonal (ACC) and meridional (Ekman) flow. While part of the circulation change can be directly attributed to the altered wind field, other factors, including surface warming, an intensified hydrological cycle and modifications to the Antarctic sea-ice, can also cause a reorganisation of the internal density field and thus the internal flow. For instance, Russell *et al.* (2006b) investigate the factors affecting the fidelity of the Southern Ocean simulations in the CMIP3 models. They find that the most important gauges of realistic circulation are the strength of the westerlies over the Drake Passage latitudes, the heat flux gradient over this region, and the salinity gradient across the ACC through the water column. The authors suggest that it is this latter property, modulated by the upwelling of North Atlantic Deep Water (NADW) to the south of the ACC, that is the most important in affecting inter-model variability in the ACC. There is modelling evidence that the future potential for the Southern Ocean to sequester atmospheric heat and gases, in climate simulations, is also strongly modulated by the present-day position and strength of the mid-latitude westerlies (Russell *et al.*, 2006a). Despite rising temperatures causing increased surface stratification, stronger westerlies and greater high-latitude divergence, help to maintain a strong connection between the surface ocean and the interior, mitigating against sequestration decreases in anthropogenic CO<sub>2</sub> due to the increased stratification. This result does not however make allowance for changes

in the natural carbon cycle. Recent modelling (Lovenduski *et al.*, 2007) and observational (Le Quere *et al.*, 2007) studies suggest that a positive SAM is actually associated with increased CO<sub>2</sub> outgassing as a result of enhanced wind-driven upwelling of old carbon-rich sub-surface waters, resulting in a potential positive feedback. This is an issue of ongoing debate (Zickfeld *et al.*, 2008; Le Quere *et al.*, 2008; Law *et al.*, 2008).

The subtropical gyre circulation is more directly controlled by the curl of the wind-stress via Sverdrup dynamics. This circulation extends to considerable depth and controls the flow pathways of not only surface waters but also thermocline, mode and intermediate water-masses. Roemmich *et al.* (2007) find an increase in the observed wind-driven transport of the south Pacific subtropical gyre since 1993, which they link to an intensification of wind stress curl to the east of New Zealand, possibly associated with the positively trending SAM. Cai *et al.* (2005) investigate projected changes to the wind-stress curl in one of the AR4 models (*CSIRO3.0*) and find an intensification of wind-stress curl over the subtropical gyres. This manifests itself as a spin-up of the gyre, with a significant increase in East Australian Current (EAC) transport and an associated enhanced warming in the Tasman Sea. A similar shift in the wind stress curls and subtropical gyres was found by Saenko *et al.* (2005) for the *CGCM3.1(T47)*.

In contrast to the clear long-term decrease in observed Arctic sea-ice cover in the Northern Hemisphere (NH, e.g., Serreze *et al.*, 2007; IPCC, 2007), SH sea-ice exhibits large interannual variations but no consistent large-scale trends (IPCC, 2007). Only at regional scales is there evidence that annual sea-ice duration and monthly sea-ice concentration have decreased (increased) in the western Antarctic Peninsula and southern Bellingshausen Sea (western Ross Sea) region since 1979 (Stammerjohn *et al.*, 2008). These changes are postulated to be related to decadal variations in the SAM and the extratropical response to the El Niño Southern Oscillation (ENSO). For the AR4 models, Parkinson *et al.* (2006) find that their ability to reproduce the observed annual cycle in sea-ice cover is better in the NH

than SH. They attribute this to a more realistic representation of the ocean circulation in the NH. Arzel *et al.* (2006) and Lefebvre and Goosse (2008a) investigate sea-ice fidelity in the AR4 model simulations and find that there is a reasonable reproduction of the observed Antarctic sea-ice trends over the 20th century by the multi-model mean, especially the decrease along the Antarctic Peninsula. Again an associated link with a positively-trending SAM is suggested (Lefebvre and Goosse, 2008a).

In this study we compare large-scale simulated ocean and sea-ice characteristics from the last two decades of the CMIP3 20th century control runs with observations. Future projections of these characteristics are also assessed for the SRES A1B scenario. The SRES A1B scenario contains the largest selection of data available for the present study. By assessing the largest possible set of models various relationships may be drawn between characteristics of the oceanic forcing (particularly pertaining to differences in wind-stress) and oceanic inter-model differences. A primary aim is to provide a self-consistent explanation for the projected changes throughout the extratropical ocean, given the projected changes to surface forcing. In section 2, we briefly describe the CMIP3 models used in our analysis. In section 2.1 we discuss the need to correct for model drift in order to investigate future projections, particularly in the deeper ocean. In section 3, we present comparisons of simulated SH properties with observations, and show the projected changes to the atmospheric forcing (section 3.1), various oceanic fields (section 3.2-3.7) and sea-ice (section 3.8). Finally in section 4, we present our conclusions and summary.

## 2. CMIP3 Models

The CMIP3 is an initiative by the World Climate Research Programme to bring together output from an unprecedented array of climate models used as part of the IPCC AR4 (for details on the initiative see Meehl *et al.*, 2005, 2007). Output is stored and disseminated by the Program for Climate Model Diagnoses Intercomparison (PCMDI). Output from

three standard experiments are used in this study for the available models. Firstly, the 20<sup>th</sup> century control run (20C3M) is an integration from 1850 to ~2000 using realistic natural and anthropogenic forcing. This integration is generally initialised from a long pre-industrial control run. For the analysis of a given variable we use all possible realisations available for the last 20 years of the 20<sup>th</sup> century (hereafter *20C*). Sensitivity studies related to the time period employed suggests that 20 years is sufficient to account for interannual variability, providing a robust mean state. Second, to investigate future changes we use output from the SRES A1B scenario (Nakicenovic *et al.*, 2000) initialised from the end of the 20C3M integrations. This scenario has increasing greenhouse forcing out to 2100, reaching double present day values, thereafter concentrations are kept constant. We analyse the last 20 years of the 21st century (hereafter *21C*). Finally, to assess model drift we use 100 years of the pre-industrial control run, corresponding to the 21st century time period but with constant pre-industrial forcing. The variables, time-spans and number of realisations are not necessarily the same across the different models or experiments used. For any given variable we generally present analyses from all available models and realisations.

The CMIP3 repository contains a large set of disparate models (although a few of the component-models are implemented in more than one model) encompassing a broad range of resolutions and incorporating a variety of different physical parameterisations. Table 1 shows model information with a focus on ocean/sea-ice components that supplement information presented in IPCC (2007). For the ocean components, resolutions vary from the eddy-permitting *MIROC3.2(hires)* model (0.28°x0.19°x47 levels) to the coarse resolution *GISS-ER* (5°x4°x13 levels). Most models employ a z-level vertical coordinate although isopycnal, sigma and various hybrid schemes are also represented. Sub-grid scale mixing parametrisation is implemented at different levels of sophistication. Most models implement some form of the 'GM' scheme (Gent and McWilliams, 1990), to account for the mixing of tracers by sub-grid-scale eddies. A major improvement over the models used for the third

IPCC assessment is that all of the models (except *MRI-CGCM2.3.2*, *INM-CM3.0* and both *CGCM3.1* models) can maintain a realistic present-day climate without the need for flux correction.

## 2.1. Model Drift

A model integrated forward in time from some set of initial conditions will tend to 'drift' until a quasi-equilibrium state is reached. The equilibration timescale is highly dependent on the model component, with the slowly ventilated deep ocean taking thousands of years to reach steady conditions. Unfortunately, it is not feasible to integrate these computationally expensive climate models for such periods and the various forced simulations are generally started from control runs that have been integrated out for a few hundred years at best. As a result, some model drift is to be expected particularly within the ocean. For many of the models the control simulations, from which the forced scenarios are initialised, are integrated out to provide an overlap with the forced runs. By subtracting out linear trends from the control integration, for the concurrent 21<sup>st</sup> century period, a first order correction for the drift is made. This assumes that any low-frequency variability in the ocean is small compared to the drift. Where possible, we apply such corrections to ocean temperature, salinity, barotropic and overturning stream functions and to any subsequent derived variables. Pre-industrial datasets are not, however, available for all model/variable combinations. In general, only a single realisation of the control integration is available to make drift corrections. However, for the *FGOALS-g1.0* model, three control realisations are available. The spatial pattern of trends in these realisations are very similar indicating that, for this model at least, the linear trend is insensitive to initial conditions and the long-term variability is adequately sampled providing a representative drift.

Fig. 1 shows the trend in the zonally averaged temperature across the 100 years of the pre-industrial control run for individual models. A sizeable drift is evident in many of the

models with regional drift sometimes exceeding  $0.5^{\circ}\text{C}/\text{century}$ . To put this into perspective, these regional drifts may exceed, both the range of natural variability (not shown) and the magnitude of projected change over the 100yrs of the forced run (Fig. 1, superimposed). This is most evident in the deeper ocean where ventilation by new water is weak and subsequently any forced change is small. In regions of strong ventilation, on the other hand, forced trends generally exceed the drift. It is clearly of great importance to take account of any model drift when investigating changes in the ocean interior particularly when analysing changes at smaller spatial scales or in the deep ocean. Averaging across the models (Fig. 1 bottom panel) shows that the overall drift is small indicating no systematic bias in the sign of the drift. Drift in the interior circulation is discussed in section 3.6.

### 3. Results

#### 3.1. Atmospheric Forcing

We begin by assessing the 'present-day' state and 21<sup>st</sup> century projections for the surface atmospheric fields that force the ocean and sea-ice. Figure 2 shows the multi-model and time-averaged  $20C$  means for these variables, the associated standard deviations across the models, the biases between the observations and multi-model mean ( $20C$ ), and the differences between  $21C$  and  $20C$ . Multi-model averages are calculated as unweighted means of all available models (unless otherwise stated), where means over multiple realisations for a given model are computed first. Associated zonal means are presented in Fig. 3.

**3.1.1. Wind Stress.** Large-scale features of the surface wind fields are well represented in all the models (Figs. 2, 3), with easterlies in the subtropics and strong westerlies at midlatitudes with maximum strengths in the Indian Ocean basin (although the maximum generally tends to extend too far east) and the most poleward position in the Pacific basin. In the multi-model mean, it is clear that the band of westerlies is situated too far equatorward, particularly south of Australasia ( $0.18 \pm 0.03 N/m^2$  compared to

$49.2 \pm 3.1^\circ S$  for the simulations and  $0.18 N/m^2$  and  $53.2^\circ S$  for the observations). Only the *CSIRO3.5* and *ECHAM4* models have more poleward positions. Projected wind-stress over the 21st century shows a robust southward displacement ( $1.0 \pm 0.3^\circ$  in the multi-model mean, Table 2) and intensification ( $8.0 \pm 0.1\%$ ) of the maximum zonal wind stress band across the models. Using a subset of 12 CMIP3 models, Fyfe and Saenko (2006) found a considerably stronger response in the position and strength of the maximum westerlies ( $\sim 1.9^\circ$  southward shift,  $\sim 15\%$  strength increase) for the more extreme A2 emissions scenario. Of the 20 models analysed here only two, the *FGOALS-g1.0* and *PCM* exhibit a northward displacement and only one, the *PCM*, simulate a weakening in the westerlies (Fig. 4b). For most models, this poleward intensification is most pronounced over the Pacific (Table 2). The wind shift projects strongly onto the positive phase of the SAM (Thompson and Wallace, 2000; IPCC, 2007). Despite large differences in model resolutions and physics, there are strong correlations between the position and strength of the maximum ( $20^\circ C$ ) wind stress (Fig. 4a) and between the associated changes in these variables over the 21st century (Fig. 4b). We also note that models with more poleward  $20^\circ C$  wind stress maxima tend to have smaller southward shifts into the future (Fig. 4c) indicating an increasing resistance to successively greater poleward wind-stress maximum migration.

**3.1.2. Wind Stress Curl.** In the open ocean, the depth-integrated meridional transport can be estimated from the curl of the wind-stress. The large-scale wind-stress curl distribution is captured by individual models, in particular the circumpolar maximum situated near  $40^\circ S$  (Figs. 2, 3). The largest positive values are seen around  $35^\circ S - 110^\circ E$ , in the southeastern Indian Ocean, consistent with Harrison (1989) and in the southeastern South Atlantic, suggesting strong transport associated with the Agulhas Current. Figure 2f shows small standard deviation in the tropics and subtropics, revealing a good agreement amongst the models where the curl magnitudes are large. The largest inter-model disagreement occurs near  $50^\circ S$  where the meridional gradient of the wind-stress curl is large.



In the multi-model mean the maximum curl is stronger than observed and situated too far to the north (Fig. 3b). Like the wind-stress, the largest biases occur south of Australia and New Zealand (Fig. 2g). The projected southward intensification of the wind-stress is mirrored by the wind-stress curl, although the maximum change occurs  $\sim 10^\circ$  further north, over the southern parts of the subtropical gyres. In the zonal and multi-model mean there is an increase of  $\sim 8.5\%$  and a poleward shift of  $1^\circ$  in the curl maximum.

### 3.1.3. Precipitation.

Large biases in precipitation exist across all the models. While the *20C* multi-model mean captures the low precipitation over the eastern side of the subtropical oceans (Fig. 2i), where subsidence occurs, the AR4 models are generally unable to correctly simulate the observed rainfall band associated with the subtropical convergence zones. As a consequence, the zonally averaged precipitation is generally underestimated over the midlatitudes, compared to the CMAP climatology (Fig. 3c). Biases in the representation of the mid-latitude convergence zones are known to be present in both general circulation models and reanalysis products (e.g. Quartly *et al.*, 2007; Taschetto and Wainer, 2008). Along the midlatitude storm track, the simulated precipitation is generally overestimated (Fig. 2i,k). It should be noted however that large disagreement also exists between observed rainfall products (Quartly *et al.*, 2007; Gruber *et al.*, 2000).

Precipitation is projected to increase at tropical latitudes associated with increased evaporation and enhanced convection in a warmer world (see changes in latent heat flux). At midlatitudes, between  $15^\circ S$  to  $40^\circ S$ , rainfall tends to decrease, particularly over the central to eastern Pacific (Figure 2l). Further south, the band of maximum precipitation across the Southern Ocean intensifies and shifts southwards, mirroring the poleward intensification of the maximum wind stress. Previous studies have reported a poleward shift in storm track location and increased storm intensity over the last few decades (e.g. Simmonds and Keay, 2000; Simmonds *et al.*, 2003; Yin, 2005). These changes in extratropical cyclones have again been associated with the SAM trend (Simmonds and Keay, 2000).

**3.1.4. Heat Flux.** Turbulent fluxes generally result in heat loss from the ocean. In agreement with observations, the largest contribution is from latent heat losses in the subtropics (see Fig. 3d) in particular over the Indian Ocean and at higher latitudes over the warm boundary currents. The latent heat loss steadily decreases south of  $15^{\circ}\text{S}$  with the reduction in SST. Sensible heat losses are generally of considerably smaller magnitude with largest magnitudes between  $20^{\circ}\text{S}$  and  $40^{\circ}\text{S}$ . Minimum heat loss is centred along  $50^{\circ}\text{S}$  (Fig. 3e) due to the enhanced poleward heat transport by the transient eddies in the atmosphere. There are a number of extreme model outliers in this term. For both turbulent latent and sensible fluxes, the largest inter-model differences are associated with discrepancies in the positions of the boundary currents and the ACC (discussed below) and in regions of coastal upwelling. Both terms show consistent low biases across most models compared to observations (although this is much improved when comparing against the reanalysis, which also uses bulk formulae to estimate fluxes). Observed fluxes are known to be poorly constrained with sizeable differences between products (Taylor, 2000).

The projections show an enhancement of the latent heat loss from the ocean particularly at lower latitudes, indicating higher evaporation in a warmer world (Fig. 2p). There is a weaker intensification in the Southern Ocean consistent with the smaller increases in SST at higher latitudes (see section 3.2). The largest regional intensification occurs in the Agulhas Current retroflection and Brazil-Malvinas confluence regions and in the Tasman Sea, again consistent with projected SST changes. While SST is generally projected to rise, air temperatures increase more rapidly. As such, there is a general reduction in the air-sea temperature gradient and an associated reduction in ocean sensible heat losses (Fig. 3e). This effect is accentuated south of  $50^{\circ}\text{S}$  where increased poleward eddy heat transport resulting from the poleward intensified wind field, contributes to increased air temperatures, and relatively weak SST increases, further reducing the air-sea temperature gradient. As a consequence only at higher latitudes is there a substantial net heat flux into the ocean (Fig.

3g).

### 3.2. Sea Surface Temperature and Salinity

Figure 5a shows the difference between observed and modelled ( $20C$ ) long-term mean SST for the multi-model ensemble. All observations of temperature and salinity (throughout the water-column) are taken from the CSIRO CARS2006 gridded dataset (Ridgway *et al.*, 2002), derived from all available historical subsurface ocean property measurements for the SH extratropics, through to 2006. While the use of profiling floats in particular is rapidly increasing the SH data coverage, high latitude observations are still sparse, particularly for sub-surface properties. The zonally averaged SST distribution (Fig. 5g) is well represented with biases, compared to observations, generally less than  $1^{\circ}C$ . Regional differences for individual models (not shown) can however exceed  $5^{\circ}C$ . While regional biases are in general considerably reduced in the multi-model mean, compared to any individual model, certain regions still retain sizeable biases, indicating locations of coherent bias over a number of the models. Strong mid-latitude meridional gradients mean that small biases in the position of the ACC translate into large SST biases. In particular, the Malvinas Confluence region is generally simulated too far to the north and removed from the continental margin, resulting in too much cold fresh water in this region, with warm salty subtropical water adjacent to the continent. A warm bias along the eastern boundaries is associated with the common problem of overly sluggish eastern boundary currents (e.g. Large and Danabasoglu, 2006). Close to steep topography (e.g. along the Chilean margin) there are also problems with the representation of upwelling favourable winds, which lead to biases in low cloud formation and radiative heat transfer Randall *et al.* (2007). These biases are common to a number of the models suggesting similar model deficiencies. The pattern of biases are reflected in the standard deviation across the models (Fig. 5c), indicating that model SST biases are also controlled, to a large extent, by biases in the circulation of the ACC and boundary currents.

Projected changes in SST are robust at a large scale, with all the models showing significant warming everywhere, except in the vicinity of Antarctica where some models show areas of weak regional cooling, particularly in the Weddell Gyre region (figure not shown). In the zonal mean, the degree of warming generally increases equatorward to about 45°S, north of which the magnitude of warming remains stable. These meridional differences are consistent with changes to the northward mid-latitude Ekman transport. Most models show an increase in the northward transport of cold high-latitude water to the south of 45°S with an anomalous decrease north of this latitude (Fig. 5e). Between 20°-45°S individual models generally show a warming of between 1.3° and 2.5°C except for the *MIROC3.2(hires)* model in which temperature increases exceed 3°C (in the zonal mean). Many of the models (e.g. *BCCR-BCM2.0*, *CGCM3.1(T63)*, *CCSM3*) show enhanced surface warming along the path of the ACC, particularly in the western Atlantic. This becomes a common feature of most of the models when subsurface warming is examined (see section 3.5). Some of the regional structure of surface warming can be associated with the distribution of the deep mixed layers. Regions associated with deep mixing generally show weaker surface warming. This is particularly evident along the southeastward band of deep mixed layers stretching across the Indian Ocean with an associated band of relatively weak warming in the ensemble mean (Fig. 5e) superimposed contours). Strongest warming is evident in the southwestern Pacific and in particular the Tasman Sea. Cai *et al.* (2005) note that this is likely due to increased transport in the EAC as part of a spin-up of the subtropical gyre.

In general, sea surface salinity (SSS) is more poorly represented than SST (Fig. 5b). Even in the zonal mean, salinity biases (compared to CARS06) can exceed  $\pm 0.5$  psu (Fig. 5h). In the tropical regions, where precipitation rates far exceed those in the extratropics, salinity biases are readily explained by discrepancies in surface freshwater fluxes (e.g., Large and Danabasoglu, 2006). However in the mid- and high-latitudes the biases are likely to also reflect discrepancies resulting in the upper ocean circulation. The multi-model mean

shows that in general SSS is too fresh at mid-latitudes, although some models do have a strong salty bias (particularly the *ECHAM4*, *IPSL-CM4* and *GISS-ER*, not shown). Also evident in many of the models are extended regions of high salinity along parts of the South American margin, again associated with poor representation of upwelling. At higher latitudes, surface waters tend to be too saline, particularly at some regions around the Antarctic margin. Unlike SST, the largest inter-model variability occurs at lower latitudes (Fig. 5d) and likely results from inter-model differences in surface freshwater fluxes. The very large inter-model variability is clearly evident in the zonally averaged profiles (Fig. 5h).

Compared to the inter-model differences and model biases, the projected changes in SSS are relatively modest. The most robust feature is a freshening of surface waters around Antarctica. This is consistent with the large-scale increase in precipitation over the Southern Ocean and enhanced runoff from Antarctic. These models do not simulate changes to land ice cover and as such a large potential source of additional freshwater runoff is likely absent. Salinity changes resulting from altered sea-ice conditions are discussed in section 3.8.

### 3.3. Mixed Layer Depth (MLD)

The SH mid-latitude oceans are home to some of the deepest, most expansive mixed layers in the world, formed through vigorous winter convection. These deep mixed layers are fundamental to the formation of Subantarctic Mode Water (SAMW) in the Pacific and Indian Oceans and of AAIW in the southeastern Pacific, and in setting thermocline properties. These water-masses are also associated with the sequestration and storage of large quantities of anthropogenic CO<sub>2</sub> (e.g. Sabine *et al.*, 2004). As noted above, the MLD distribution also affects the simulated pattern of projected surface warming. A realistic representation of MLD is therefore a vital component of any coupled climate model.

In order to compare model and observed depths we estimate the maximum annual mixed layer depth, calculated as the depth where the buoyancy difference between the near surface

and the mixed layer base exceeds  $0.003\text{ms}^{-2}$ . While many of the models actually diagnose MLD via a variety of schemes (see for example Griffies *et al.*, 2008), this diagnostic is unavailable as part of the PCMDI repository and the use of a common definition throughout means that we are comparing like with like. Deep observed MLD stretches in a band from the central Indian Ocean, southeastwards towards the Drake Passage, with weaker enhanced convection in the southwest Atlantic (Fig. 6 final panel). The deepest mid-latitude mixed layers are evident south of Australia and New Zealand and in the eastern Pacific. Very deep mixing also occurs in the Weddell Sea and at other locations around the Atlantic margin, although little in-situ data is available to constrain the observational products used in the estimation of 'observed' MLD.

Most models simulate the enhanced mid-latitude mixed layers forming a southeastward band across the Indian and Pacific regions. The *GISS-ER* shows the greatest mid-latitude MLD bias across all basins with basin-wide zonally-averaged depth too great by a factor of 3. The *FGOALS-g1.0* model has only a weakly enhanced mid-latitude MLD, reaching to only  $\sim 250\text{m}$ , where in the observations depths exceed  $700\text{m}$  in places. Figure 7 shows the surface area within the mid-latitude domain that has MLD within (20m) binned ranges for the *20C* and *21C*, with the observed distribution superimposed for reference. The right-hand tails of the distributions represent the important deepest mixed layers associated with water mass formation. Many of the models (particularly *BCCR-BCM2.0*, *CSIRO3.5*, *GFDL-CM2.0*, *FGOALS-g1.0*, *MIROC3.2(hires)*, *MRI-CGCM2.3.2* and *UKMO-HadCM3*) lack the deepest mixed layers ( $>400\text{m}$ ) evident in the observations, although this is often compensated by more substantial areas of medium depth (200-400m) MLD. On the shallow end of the distribution, nearly all models lack a substantial area of very shallow ( $<40\text{m}$ ) mixed layers. It should be stressed that the lack of observational constraints could affect both ends of the observed distribution. Despite large regional inter-model differences, integrated over the full mid-latitude domain, the volume of water contained within the winter MLD envelope varies

by less than 30% from observed ( $\sim 1.4 \times 10^{16} m^3$ ) across all models, except the *CSIRO3.0* and *GISS-ER* whose volume is too large by  $\sim 50\%$  and  $150\%$ , respectively.

A comparison of the surface area of deep mixed layers ( $>200m$ ) in the Pacific versus the Indian basin (where MLD reach considerable depths) across the models reveal a significant correlation ( $r=0.8$  using all models), i.e. a model with a deep bias in the Pacific will also tend to have a deep bias in the Indian basin. This suggests that a large proportion of the model MLD bias is unrelated to local forcing and instead results from different mixing parameterisations or large-scale forcing biases. In an inter-comparison of ocean-ice GCMs forced using a common (CORE) climatology, Griffies *et al.* (2008) suggest a large component of the inter-model variability might be explained by differences in the treatment of the neutral physics scheme (Gent and McWilliams, 1990) rather than different vertical coordinate systems. The standard deviation across the models indicate that inter-model variability is associated with the depth of the deepest mixed layers in the eastern Pacific, but is more related to the position of these layers in the east Indian basin. Very large variability also exists around the Antarctic margin, as some models exhibit very deep MLD while others have essentially no deep mixing.

Figures 6 and 7 also show the projected changes for the 21st century. In general, there is a consistent shoaling of the deepest mixed layers. Similarly around Antarctic there is a large shoaling of deep mixed layers. Considering the mid-latitude domain only (see Fig. 7), the total volume contained within the MLD is projected to decrease for all the models, ranging from a drop of  $\sim 5\%$  for *GFDL-CM2.0* and *MRI-CGCM2.3.2* to over 20% for *CNRM-CM3* and *ECHO-G* models. The anomalous projected mid-latitude shoaling is situated slightly south of the maximum MLD, in the multi-model mean, indicating a small poleward shift in their position in addition to the shoaling.

### 3.4. Horizontal Circulation

A major component of the oceanic circulation is driven by the wind. As a result, the robust shifts in Southern Hemisphere winds, both observed and simulated, are likely to drive major changes to the ocean circulation. Modified heat and moisture fluxes associated with enhanced greenhouse forcing will also modify the circulation via buoyancy changes.

The barotropic stream-function represents the depth integrated ocean circulation. Figure 8 shows the multi-model mean barotropic stream-function and 'observed' stream-function derived from the SODA reanalysis. The main features are well captured in the multi-model mean and across individual models (not shown). The simulated ACC has the characteristic southeastward pathway from the western Atlantic through to the eastern Pacific superimposed with regional meandering as a result of topographic steering (particularly over the Macquarie Ridge system and the Kerguelen Plateau) and a contraction in the flow through the Drake Passage followed by a sharp northward excursion. The Weddell Gyre is realistically situated, albeit slightly weaker than observed, however the Ross Gyre is very weak and confined too far to the south in the ensemble mean. The simulated subtropical gyre in the Indian Ocean basin is generally situated too far to the north - consistent with the equatorward bias in the wind-stress curl, and the western boundary currents are overly sluggish, a common feature of coarse resolution models. The individual models for the most part, capture the general lateral circulation features described for the multi-model mean i.e. western intensification in the subtropical gyre and a strong circumpolar circulation, although, there are significant regional inter-model differences.

In a selection of the AR4 models, Fyfe and Saenko (2006) found that associated with the poleward shift in the mid-latitude westerlies, over the 20th and 21st centuries, there is a consistent poleward intensification of both the ACC and high-latitude meridional Ekman flow. They fit the depth integrated zonal velocity and the zonal wind stress to a Gaussian distribution at each longitude, to obtain an estimate of the latitude and magnitude of the



maximum flow. While this method works well for the wind-stress (see their Fig. 1), we find that the structure of the ACC is less amenable to this approach as the distribution is often heavily skewed or has multiple cores (commonly associated with Subantarctic and Polar fronts in observations). We implement an alternative approach whereby, at each longitude, a simple weighted average of latitude (by zonal flow strength) is calculated to obtain an estimate of the average core position. Core strength is then simply the mean depth-integrated velocity over these values. While this strength estimate does not correspond to the maximum core strength (as it includes everything to 50% of the maximum) it provides a representative magnitude for the ACC core.

Figure 9 shows the position of the ACC core for the different models, with the observed (SODA) ACC core superimposed. Two of the models the *CSIRO3.0* and the *GISS-ER* have the largest overall biases, with the ACC core over  $5^\circ$  too far south (in the zonal mean), but with regional differences exceeding  $10^\circ$ . Conversely the *IPSL-CM4* and *MIROC3.2(hires)* have ACC cores in excess of  $3^\circ$  too far to the north. The multi-model mean of ACC position (Fig. 10), however, closely tracks the observed pathway across most of its domain. The largest bias, is evident in the western Atlantic where the ACC for the majority of models tracks too far to the north. This bias was also manifest in the SST (Fig. 5, section 3.2) where a large cold bias occurs as high-latitude water is advected too far northward.

Figure 9 also shows the projected change in the position of the ACC core over the 21st century. Our findings, which comprise an expanded set of 15 models, are essentially in agreement with the 8 models analysed by Fyfe and Saenko (2006). The majority of models show an overall poleward contraction of the ACC core, although a number of models have regions where the core moves equatorward. Four models show a net equatorward movement (*GISS-ER*, *CSIRO3.0*, *FGOALS-g1.0* and *CNRM-CM3*, although the change is small in the first two). The *FGOALS-g1.0* change is associated with the only net northward wind shift across the models (Fig. 4f) and the *CNRM-CM3* change is related to a large northward

movement in the mid Pacific, where the core is weak and poorly defined.

The model with the largest southward shift in the maximum westerlies (*ECHO-G*) also shows the greatest overall (zonally averaged) ACC shift (almost  $3^\circ$  in the zonal mean). Across the models there is a strong link between the magnitude of the wind-stress shift and the ACC shift, with a correlation of  $r=0.7$  ( $p=0.01$ ; Fig. 4). A regression analysis indicates that the position shift in the ACC is approximately half that of the wind stress shift. This may relate to the fact that the ACC flow is somewhat constrained by contours of  $f/H$  ( $H$ =bottom depth), although the strength of flow along lines of constant  $f/H$  may change, leading to a meridional shift in the ACC core. The multi-model average shows a poleward shift at all longitudes, with a zonally averaged shift of  $\sim -0.6^\circ \pm 0.4^\circ$ .

In addition to the poleward shift in the ACC, Fyfe and Saenko (2006) found a consistent strengthening of the maximum depth-integrated flow at all longitudes. While we also find an increase in the strength of the ACC over the majority of the models, there is a high degree of regional and inter-model variability. The CSIRO3.0 model is again an outlier and shows a zonally-averaged weakening of the ACC core strength with a reduction of over 5%. All other models show an increased core magnitude with many models having projected increases exceeding 10% (Fig. 4g). The change in core strength does not necessarily correspond to a change in ACC transport, however, as the total flow width may also contract or expand. An important and well-measured metric for ACC flow is the volume transport passing through the Drake Passage. Table 3 shows the *20C* and *21C* mean volume transports. Common estimates of Drake Passage transport are  $\sim 135\text{Sv}$  (e.g. Cunningham *et al.*, 2003). Model ability to capture this transport varies considerably with present day estimates ranging from less than  $50\text{Sv}$  for *IPSL-CM4* to in excess of  $300\text{Sv}$  for CSIRO3.0. Projected changes in the transport are also highly variable with a range of almost 30% increase for the *INM-CM3.0* to almost 30% decrease for the *CNRM-CM3*. There is essentially no projected change in the ACC core position passing through the Drake Passage for any of the models.

Cai *et al.* (2005) find that for the *CSIRO3.0* there is a projected spin-up of the mid-latitude gyre circulation into the future, particularly along the path of the EAC, as the SAM trends towards an increasingly positive state. Figure 9 shows selected stream-function contours representative of the position of the mid-latitude gyres for the *20C* and *21C* periods. Zonally averaged stream-function and wind-stress curl are also shown for the individual models. As expected, a significant link exists between the position of the wind-stress curl minimum and the cores of the subtropical gyres across the models (Fig. 4). A southward shift occurs across all the models over the 21st century. A strong correlation exists across the models between the shift in the zonally-averaged position of the wind-stress curl core and the associated change in the position of the zonally-averaged stream-function core (Fig. 4 ;  $r=0.8$ ,  $p=0.01$ ). As with the shift in the position of the ACC, a regression analysis indicates that the shift in the wind stress curl position is approximately twice the magnitude of shift in the position of the gyre cores.

In order to provide a measure of the gyre strength, Fig. 11 tracks the strength (calculated as the component of the depth integrated core strength travelling along the coast) of the western boundary current core for the three subtropical gyres. The projected changes have quite different characteristics within the different basins. Along the EAC there is often a strong increase in flow at higher latitudes with a compensating decrease at lower latitudes, indicative of a southward shift in the circulation. There is no robust increase in the maximum flow however, although, as noted by Cai *et al.* (2005), the *CSIRO3.0* does show an enhanced flow into the Tasman Sea region. Along the Brazil Current, on the other hand, as well as a southward shift there is a robust increase in the strongest flow, indicative of a spin up of the gyre. In the Agulhas region changes are less robust, with some models showing weak projected reductions in the higher latitude flow.

### 3.5. Heat Content

Figures 9 and 10 also show the change in the depth integrated heat content for individual models and the ensemble mean, respectively. Heating appears to be strongly modulated by changes in the lateral circulation. For most models, the largest heating occurs at midlatitudes, broadly constrained by the ACC to the south and the eastward limbs of the subtropical gyres to the north. This is clearly seen in the multi-model mean, where both the ACC core and the subtropical gyres show obvious shifts to the south.

Were the change in heat content mainly attributable to altered surface heat fluxes the mid-latitude region might be expected to be an area of enhanced warming as the deep overturning would mix additional surface heat into the interior. However, the largest heat content changes occur in the western Atlantic and Indian Ocean regions, where the MLDs are generally shallower than in the eastern Indian and Pacific regions. Furthermore the primary input of additional surface heating occurs to the south of  $50^\circ$  (Fig. 3f). The western Atlantic and Indian Ocean regions are however generally associated with the strongest meridional temperature gradients (figure not shown). Thus any poleward shift in the circulation would preferentially enhance heat content change at these locations.

### 3.6. Vertical Circulation

The extratropical large-scale Eulerian meridional overturning circulation (MOC) is characterised by three main cells: the Antarctic overturning cell, which is related to the sinking of AABW; the abyssal cell, that extends north of approximately  $40^\circ\text{S}$  representing the northward flow of AABW and the compensating southward flow of lower Circumpolar Deep Water (CDW) and lower NADW; and the Deacon Cell, that represents the upwelling of upper CDW and northward Ekman transport. The Deacon cell overturning should be interpreted with care as by construction a part of this cell strength is an artifact of zonal averaging in a region where isopycnal depths change with longitude (Döös and Webb,

1994). The MOC diagnostic is not readily calculable in the observations as it requires a full 3-dimensional knowledge of the ocean meridional velocity fields.

Figure 12 shows the *20C* mean state MOC overlaid on the projected 21<sup>st</sup> century changes. The three cell configuration is clear in the multi-model mean but is also present in all the models except for the *INM-CM3.0* where, for example, a negative subsurface cell exists at the characteristic position of the Deacon cell. In the *IPSL-CM4* model both the Deacon and Antarctic cells are situated in a much more northward position than the other models. This bias is associated with the largest northward zonal wind-stress (and ACC) position (Fig. 4) and manifests itself as the most extreme mid-latitude cold bias (Fig. not shown). Dynamical reasons would suggest a relationship between wind stress position/strength and overturning position/strength, via changes in the strength and position of Ekman pumping and indeed significant correlations exist across the models. The standard deviation in MOC across the models (Fig. 12) indicates largest inter-model variability associated with the strength of the Deacon circulation but also in the magnitude and position of the deep water exchange. By comparing the mean and standard deviation of individual cell strengths (Fig. 13) we also find significant inter-model differences in the weaker cells. In particular, the standard deviation and mean of the Antarctic cells are of comparable magnitude. These differences are partly associated with the strength of high-latitude density stratification. A significant correlation ( $r \sim -0.7$ ) exists between the mean vertical density gradient over the top 100m, south of 60°S, and AABW overturning across the models (excluding *INM-CM3.0*). This implies that models with weak stratification, which also tend to have low vertical resolution, tend to exhibit strong AABW overturning.

The sign of the projected changes for the three overturning cells are, however, robust across almost all the models. In all but the *CSIRO3.5* model, there is a spin-up of the Deacon Cell (Fig. 13). The behaviour of the outlier is related to the equatorward shift of the zonal wind stress in the Pacific sector (Table 2). The projected multi-model mean

increase of this cell is  $\sim 4\text{Sv}$  (Fig. 12), indicating an intensified upwelling of relatively warm and saline upper CDW. Significant correlations exist between the change in both the position and strength of the maximum zonally averaged wind-stress and the corresponding changes in the position and strength of the Deacon cell across the models ( $r > 0.75$ ,  $p < 0.007$  for position and  $r > 0.8$ ,  $p < 0.001$  for strength, excluding *INM-CM3.0*). Despite substantial differences in resolution, bathymetry and physical parameterisations, inter-model differences in the mid-latitude MOC is primarily determined by biases in wind field. Previous studies have shown a strong short-term response in the Deacon Cell driven by changes in the SAM (Hall and Visbeck, 2002; Sen Gupta and England, 2006). For a positive SAM this cell spins up and shifts polewards. The long-term trend towards a more positive SAM phase seen in the models would therefore be consistent with these projected changes.

In the multi-model mean, the AABW cell weakens by  $\sim 2\text{Sv}$  (Fig. 13). This spin down is consistent with the projected surface intensified buoyancy gain around the Antarctic margin. A comparable reduction in the abyssal cell strength reflects its response to the weakening AABW formation and subsequent outflow. A weak correlation exists between changes to the abyssal and AABW cell strengths. As an aside, Fig. 13 also shows the overturning calculated without any correction for drift. It is evident that for some models drift explains an important proportion of the raw MOC change, particularly in the abyssal cell. Fig. 12 also shows the standard deviation in the projected overturning changes. Large differences in the projected response are associated with the Deacon cell and inflow of deep water. There are also large surface intensified inter-model differences along  $40^\circ\text{S}$  presumably associated with wind-driven differences in the convergence zone.

### 3.7. Internal Properties

Figure 14 shows the projected changes to the zonally averaged potential temperature. A general warming pervades the extratropics, with enhanced surface warming, particularly

between  $40^\circ$  and  $60^\circ\text{S}$  extending to mid-depth and for almost all models an enhanced abyssal warming near the Antarctic margin. The weakest warming, and in some models a weak cooling, occurs at mid-depth north of  $40^\circ\text{S}$ .

It was suggested in section 3.4 that a large component of the change in heat content can be attributed to the poleward shift of the mid-latitude circulation. Superimposed on Fig. 14 are contours indicating the change in temperature that would result from a  $1^\circ$  southward translation of the  $20^\circ\text{C}$  temperature distribution. At midlatitudes, as far north as  $20^\circ\text{S}$ , and primarily for the upper 1000m there is a very close correspondence between the projected warming and the warming that would result from a pure southward shift. This technique was used by Alory *et al.* (2007) to show that projected warming in the Indian Ocean could be explained, in part, by a simple southward translation of the temperature field. A recent analysis of upper Southern Ocean warming by Gille (2008) over the latter part of the 21st century, also supports the idea that the warming trend is intimately tied to a southward shift in the ACC.

The corresponding changes in salinity across the models (Fig. 15) are more varied. However, certain general features are evident. There is a freshening signal that tracks the upper part of the AAIW salinity minimum and at lower latitudes in the thermocline. Furthermore, most of the models show a saline anomaly in the surface layer at lower latitudes. At locations associated with upwelled CDW, there is generally a poleward intensified salination (except in the *CNRM-CM3* and *CSIRO3.0*) which in some models (e.g. *CGCM* models, *MIROC3.2(hires)*) feeds into the lower layers of AAIW. In most models, abutting this region of salination, at mid depths and north of  $40^\circ\text{S}$  is a freshening signal that coincides with the region of cooling (or relatively weak warming) in Fig. 14. This signal is most prominent in the Atlantic Basin (Fig. 16) indicating that these changes are associated with a modification in the southward export of NADW. In other basins, changes in this region are weak, consistent with areas of old, poorly ventilated waters (e.g. Pacific

Deep Water) where recent surface changes would not have penetrated.

Unlike temperature, which possesses a strong monotonic meridional gradient at all longitudes, zonally averaged salinity changes are less clearly attributable to a southward shift in the wind driven circulation. Other factors are evidently more important in part as salinity is much more spatial heterogeneous than temperature. Only in the upper ocean near  $40^{\circ}\text{S}$ , where there are strong meridional salinity gradients, is there an obvious contribution by this shift. This pattern originates in the Atlantic region (Fig 16) where, as noted, there is a large poleward shift and a spin-up of the subtropical gyre. The projected salination and warming signal seen in most models south of  $40^{\circ}\text{S}$  reflect changes in CDW. While changes in CDW could occur through property changes in NADW or via changes in the rate of diapycnal mixing with neighbouring AAIW/AABW (Santoso *et al.*, 2006), such mechanisms would not result in changes consistent with those projected. Instead, the dominant mechanism appears to be an increased southwards and upwards transport of freshwater and heat, within the CDW, associated with the spin-up of the Deacon circulation.

North of  $40^{\circ}\text{S}$  the freshening of the deep water is consistent with the slowdown of the North Atlantic overturning cell that transports warm and salty water southwards. This signal appears to be decoupled from changes in the Southern Ocean, south of the region of NADW separation. At shallower depths enhanced advection of warm and salty water into the Southern Ocean occurs primarily in the Atlantic Basin via the poleward intensified Brazil Current (Fig. 16) across the Brazil-Malvinas confluence where strong T-S gradients mean that the poleward intensification of the circulation generates substantial T-S changes. This warm salty signal connects into the upper CDW. This is consistent with a modelling study by Santoso *et al.* (2006) who showed that a significant portion of upper CDW  $T - S$  variability originates within the Brazil-Malvinas Confluence via meridional advection. The anomalous signal then propagates into the Southern Ocean CDW via the ACC.

As noted in section 3.6, in polar regions, AABW overturning is generally projected to



weaken. This is consistent with an increase in buoyancy in the surface regions (see below) as a result of surface warming, increased surface freshwater flux and changes to the seasonal cycle of sea-ice (see section 3.8). Combined with a generally negative vertical gradient in the mean-state  $T$  and  $S$  at polar latitudes (i.e. colder and fresher conditions near the surface), this slow-down of the overturning translates into a warm, saline signal close to the Antarctic margin. These modifications reinforce the changes in  $T$ - $S$  noted for the CDW. Changes, particularly in upper ocean temperature and salinity, result in robust large-scale reductions in potential density (Fig. 17). These changes are most pronounced towards the surface, resulting in a large-scale increase in the stratification of the Southern Ocean. This is consistent with the findings of Lefebvre and Goosse (2008b) who show a robust increase in the density gradient in the upper ocean for the CMIP3 models. At midlatitudes, as well as a poleward shift in the steep isopycnals, there is also an increase in the isopycnal gradient, consistent with the simulated acceleration of the zonal flow, through the thermal wind balance and a strengthening of the frontal gradients (Wainer *et al.*, 2004). Figure 17 also indicates the regions where the density changes are primarily controlled by salinity. This occurs primarily around Antarctica, where there is an increased surface freshwater input. Salinity also plays an important role at mid-depth in the subtropics, driven by changes in the subduction of freshwater into upper intermediate water.

### 3.8. Sea-Ice

For completeness we briefly discuss the fidelity and projections associated with sea-ice. All models except for the *FGOALS-g1.0* have a reasonable representation of the seasonal cycle in the sea-ice concentration (SIC) surrounding Antarctica sea-ice. This outlier has a highly unrealistic seasonal cycle (with double the integrated SIC in wintertime) as a result of high levels of numerical filtering applied at high latitudes (Yu *et al.*) and is excluded from the multi-model analysis. Simulated maximum SIC generally occurs between August

and October and minimum extent between January and March, in line with observations. During wintertime, all models except the *CGCM3.1(T63)* (which strongly overestimates SIC) are within 30% of the observed total concentration. During summer, a number of models have very low ice concentrations, in particular *CNRM-CM3*, *MIROC3.2(hires)*, *MIROC3.2(medres)* and *IPSL-CM4* have between 6 and 30% of the observed amount. Holland and Raphael (2006) look at the representation of sea-ice in six of the AR4 models and find little systematic bias in regional SIC across the models. This is borne out to some extent by the larger ensemble set evaluated here. The spatial patterns of the multi-model SIC are in reasonable agreement with observations in both seasons (Fig. 18).

The sea-ice trends into the future are robust across all simulations. All the models show a loss of sea-ice cover over the 21st century in both summer and winter (Table 4). The reduction in the integrated SIC ranges from 10% (*ECHO-G*, *cCGCM3.1(T47)*) to almost 50% (*CNRM-CM3*, *BCCR-BCM2.0*), during winter. For the majority of models, larger fractional losses in summer ranges from 33% in the *CSIRO3.0* to almost complete loss of sea-ice cover in the *MIROC3.2(hires)*. Using a small subset of the AR4 models, Holland and Raphael (2006) found a possible link between the zonally averaged meridional sea level pressure (SLP) gradient at 60°S for April to June and sea-ice extent. In our larger sample (15 models) this relationship does not appear to hold. In addition, no significant correlation was found between ice extent and the position of the SLP minimum, or ice area and zonal wind-stress at 60°S.

Table 4 also shows the changes in integrated sea-ice volume (SIV). Again there is a robust decrease in volume across the models during both seasons. For the majority of models the fractional decrease in volume is larger than the fractional change in integrated SIC, indicating that the average ice-thickness is also reducing. The multi-model mean (Fig. 18) indicates that for the winter season, substantial sea-ice loss occurs at all longitudes with the greatest loss occurring in the western Antarctic particularly on the outer edge of the

Weddell region ( $0^{\circ}$ - $30^{\circ}$ W) and between  $90^{\circ}$ - $150^{\circ}$ W. In summer, the greatest ice loss is to the east of the Antarctic Peninsula. Arzel *et al.* (2006) suggests an increase in the seasonal cycle of sea-ice, over the 21<sup>st</sup> century as the percentage decrease in both integrated SIC and SIV is greater in summer than winter. However, the much larger quantity of ice present in the winter means that in real terms there is actually a robust reduction in the seasonal change in integrated SIC (-23% in the ensemble mean) and SIV (-30%) across the models. A reduction in winter ice formation would reduce both the wintertime brine rejection adjacent to Antarctica, and also the subsequent formation of freshwater during the melt season, which is subsequently advected northwards. The net result would be a relative freshening close to the margin (less brine rejection) and more saline conditions north of the ice edge (from reduced freshwater export).

#### 4. Summary and Conclusions

Output from an ensemble of state-of-the-art coupled climate models used as part of the IPCC AR4 process are compared with recent observations and are investigated for projected changes over the 21<sup>st</sup> century. Our goal is to provide a overarching description of large-scale changes to the SH extratropical ocean in light of changes projected to occur in the atmosphere. Unlike in the tropics, changes to these higher-latitude oceans can be considered as largely atmospherically forced phenomena (at least to first order) rather than having to consider highly coupled air-sea interactions.

There exists large variability across the model set, as a result of different model configurations (e.g. resolution and bathymetry) and different treatment of the underlying physics (Table 1). Nevertheless, except in certain regions, biases are often not systematic and a simple, unweighted multi-model mean provides a realistic representation of the observed system. Moreover, future projections tend to be qualitatively robust across most models. It is apparent that a large component of individual model bias, associated with

ocean dynamics and thermodynamics, results from biases in the overlying wind field. Further, it is changes to the wind field that can explain many of the modifications projected for the ocean. Over the 21<sup>st</sup> century, both the wind-stress maximum (at  $\sim 50^\circ\text{S}$ ) and the wind stress curl (at  $\sim 40^\circ\text{S}$ ) are projected to intensify and shift southwards. At the same time there is an intensification of the hydrological cycle with increased precipitation in the tropical and mid-to-high latitude regions and reduced precipitation in the subtropics. At midlatitudes this is related to a poleward intensification of the mid-latitude precipitation linked to a shift in the Southern Hemisphere storm track. These wind-induced modifications are consistent with an increasingly positive SAM. The pattern of heat flux change is more complex. Overall, there is a shift in the balance of turbulent heat fluxes from the ocean to the atmosphere: a reduction in sensible heat loss is counteracted by an increase in latent heat loss, although regional variations abound. In general, there is an increased radiative flux into the ocean, most pronounced at high latitudes where there is also a reduction in summer albedo. Most of the additional heat entering the SH oceans does so to the south of  $50^\circ$ .

Figure 19 shows a schematic diagram of the more robust projected changes across the models. Associated with the southward intensification of the westerlies there is a southward shift in the position of the ACC core. As the ACC position is strongly affected by bathymetry, its poleward shift is, in general, only about half as large as the shift in the position of the wind-stress. Sen Gupta and England (2006) showed modest changes in the barotropic flow of the ACC due to changes in surface slope associated with high frequency SAM variability. At these short timescales they found little change in flow associated with modifications to the ocean density structure. For the long-term changes discussed here, a steepening of isopycnals is evident, that is consistent with an intensified ACC, driven by changes in surface Ekman pumping and an associated spin up of the Deacon circulation. At lower latitudes the maximum wind-stress curl also moves southward and intensifies, driving

a southward shift in the position of the subtropical gyres. Only in the Atlantic basin, where the gyre core has a more southerly mean position, is there evidence of a robust increase in the depth-integrated flow of the western boundary current. The overall southward shift of the lateral circulation manifests itself as an increase in the heat content of the water column, primarily between the lower limb of the gyres and the core of the ACC. This can be understood as a simple poleward displacement in the temperature distribution in a region where the meridional temperature gradients are large. The largest increase in heat content occurs in the western Atlantic where in addition to the circulation shift there is increased transport of warm water in the boundary flow.

Around the Antarctic margin enhanced heating from above and below results in a melt back of the summer and winter sea-ice. As noted, this feeds back to the radiative balance through a decrease in the surface albedo. The seasonal cycling of sea-ice acts as a factory for the production of fresh water during the summer melt, that is advected northwards in the Ekman flow, and saline water during wintertime ice-formation and brine rejection, that is exported to depth. A reduction in the output of the factory, i.e. by the reduced projected seasonal cycle in ice volume, will therefore result in relatively fresher conditions at high latitudes and saltier conditions north of the ice-edge. The latter process appears to be completely offset by increased high latitude precipitation over the ocean and increased runoff from water precipitated onto Antarctica. The surface freshening and surface intensified warming is consistent with a weakening of AABW formation, which in turn is manifest as a warming signal close to the Antarctic margin that reaches abyssal depths. Possible changes to the Antarctic ice-sheet are not accounted for in IPCC AR4 models.

While the poleward displacement of the circulation can account for much of the temperature distribution change, it explains less of the salinity changes. Instead, surface changes are closely tied to the projected intensification of the hydrological cycle and of Ekman transport. This is consistent with the idea that inter-model variability in SST is

primarily driven by circulation differences, while SSS variability is more related to differences in freshwater fluxes (section 3.2). Only in the Atlantic is there a clear 'circulation shift' signal in the salinity as the Brazil-Malvinas Confluence, which acts as a barrier between salty subtropical and fresh Southern Ocean water, moves southwards. In the interior, south of  $\sim 40^\circ\text{S}$ , there is a subsurface increase in salinity that is consistent with an intensified southward and upward movement of relatively warm and saline CDW, associated with the more rapid Deacon Cell overturning. This is further enhanced by an injection of warm and saline upper CDW entering from the Atlantic sector as a result of the southward intensified Brazil Current coupled with the large meridional T-S gradients in the Brazil-Malvinas Confluence Zone. At lower latitudes, primarily in the Atlantic basin, there is a freshening signal at depth, consistent with the projected slow down of relatively salty NADW circulation. Throughout the extratropics there is an increase in stratification driven by a surface intensified density reduction. At high latitudes this is primarily a result of salinity changes, while at lower latitudes it is primarily driven by temperature changes. This results in a large scale shoaling of the deep mixed layers at mid-latitudes.

While this paper provides a consistent picture of future changes, our analysis is essentially qualitative. A more quantitative accounting of the various changes must follow. For instance by looking at changes along density surfaces (e.g. Bindoff and McDougall, 1994) the contributions of heat and freshwater fluxes and pure displacements of isopycnals via "heave" effects can be disentangled. This will be the subject of future work. We also note two caveats in interpreting projections from the AR4 models. First, the dynamics of the ocean circulation still lacks certain physical processes. For example, sub-grid scale eddies that could be critical to realistically capturing future oceanic changes. Recent modelling and observational studies (e.g. Meredith and Hogg, 2006) suggest that a proportion of the additional energy entering the ocean via a momentum flux would energise the eddy field rather than enhance the circumpolar circulation. Secondly, recent evidence based on

models with more realistic depictions of the stratosphere (Son *et al.*, 2008) suggests that the poleward intensification of the wind field may halt, or even reverse, at least during austral summer, by the recovery of stratospheric ozone over Antarctica. Only a few of the AR4 models incorporate any form of ozone recovery (see Fig. 4) and these tend to underestimate the resulting modification in the atmospheric circulation compared to models with a more realistic stratosphere (Son *et al.*, 2008). Thus, a definitive assessment of the changes in certain oceanic properties are essentially beyond the scope of the AR4 models. Nevertheless, it is encouraging to find that despite sometimes large inter-model differences, systematic biases are generally small and projected changes are for the most part qualitatively robust.

**Acknowledgments.** We would like to acknowledge the effort of all the groups involved in putting together the CMIP3 repository. This work also like to thank Olivier Arzel and our two anonymous reviewers for their useful comments. This research was supported by the Australian Research Council ARC.

## References

- Alory, G., S. Wijffels and G. Meyers, 2007: Observed temperature trends in the Indian Ocean over 1960-1999 and associated mechanisms . *Geophysical Research Letters*, **34**, doi:10.1029/2006GL028044.
- Aoki, S., N. L. Bindoff and J. A. Church, 2005a: Interdecadal water mass changes in the Southern Ocean between 30°E and 160°E . *Geophysical Research Letters*, **32**, L07607, doi:10.1029/2004GL022220.
- Aoki, S., S. R. Rintoul, S. Ushio, S. Watanabe and N. L. Bindoff, 2005b: Freshening of the Adelie Land Bottom Water near 140°E . *Geophysical Research Letters*, **32**, L23601, doi:10.1029/2005GL024246.
- Arzel, O., T. Fichefet and H. Goosse, 2006: Sea ice evolution over the 20th and 21st centuries as simulated by current AOGCMs . *Ocean Modelling*, **12**, 401–415.
- Beckmann, A. and R. Döscher, 1997: A method for improved representation of dense water spreading over topography in geopotential-coordinate models . *Journal of Physical Oceanography*, **27**, 581–591.
- Bindoff, N. L. and T. J. McDougall, 1994: Diagnosing Climate Change and Ocean Ventilation Using Hydrographic Data . *Journal of Physical Oceanography*, **24**, 1137–1152.
- Bindoff, N. L. and T. J. McDougall, 2000: Decadal changes along an Indian Ocean section at 32S and their interpretation . *Journal of Physical Oceanography*, **30**, 1207–1222.
- Blanke, B. and P. Delecluse, 1993: Variability of the Tropical Atlantic Ocean Simulated by a General Circulation Model with Two Different Mixed-Layer Physics. *Journal of Physical Oceanography*, **23**, 1363–1388.
- Bryan, K. and L. J. Lewis, 1979: A water mass model of the world ocean . *Journal of Geophysical Research*, **84**, 2503–2517.



- Bryden, H. L., E. L. McDonagh and B. A. King, 2003: Changes in ocean water mass properties: Oscillations or trends . *Science*, **300**, 2086–2088.
- Cai, W., G. Shi, T. Cowan, D. Bi and J. Ribbe, 2005: The response of the Southern Annular Mode, the East Australian Current, and the southern mid-latitude ocean circulation to global warming . *Geophysical Research Letters*, **32**, L23706, doi:10.1029/2005GL024701.
- Cunningham, S. A., S. G. Alderson, B. A. King and M. A. Brandon, 2003: Transport and variability of the Antarctic Circumpolar Current in Drake Passage. *Journal of Geophysical Research*, **108**, 8084.
- Döös, K. and D. J. Webb, 1994: The Deacon Cell and the Other Meridional Cells of the Southern Ocean. *Journal of Physical Oceanography*, **24**, 429–442.
- Friedlingstein, P., 2008: A steep road to climate stabilization. *Nature*, **451**, 297–298.
- Fyfe, J. C. and O. A. Saenko, 2006: Simulated changes in the extratropical Southern Hemisphere winds and currents . *Geophysical Research Letters*, **33**, L06701, doi:10.1029/2005GL025332.
- Fyfe, J. C., O. A. Saenko, K. Zickfeld, M. Eby and A. J. Weaver, 2007: The role of poleward-intensifying winds on Southern Ocean warming . *Journal of Climate*, **20**, 5391–5400.
- Gent, P. R., W. G. Large and F. O. Bryan, 2001: What sets the mean transport through Drake Passage? . *Journal of Geophysical Research*, **106**, 2693–2712.
- Gent, P. R. and J. C. McWilliams, 1990: Isopycnal mixing in ocean circulation models. *Journal of Physical Oceanography*, **20**, 150–155.
- Gille, S. T., 2002: Warming of the Southern Ocean since the 1950s . *Science*, **295**, 5558, 1275–1277.

- Gille, S. T., 2008: Decadal-Scale Temperature Trends in the Southern Hemisphere Ocean. *Journal of Climate*, **21**, 4749–4765.
- Gillett, N. P. and D. W. J. Thompson, 2003: Simulation of recent Southern Hemisphere climate change. *Science*, **302**, 273–275.
- Griffies, S. M., 1998: The Gent-McWilliams Skew Flux. *Journal of Physical Oceanography*, **28**, 831–841.
- Griffies, S. M., A. Biastoch, C. Boening, F. Bryan, E. P. Chassignet, M. H. England, R. Gerdes, H. Haak, R. W. Hallberg, W. Hazeleger, J. Jungclaus, W. G. Large, G. Madec, B. Samuels, M. Scheinert, A. Sen Gupta, C. Severijns, H. Simmons, A.-M. Treguier, M. Winton, S. Yeager and J. Yin, 2008: Coordinated Ocean-ice Reference Experiments (COREs). *Ocean Modelling*, (In Press).
- Gruber, A., X. Su, M. Kanamitsu and J. Schemm, 2000: The comparison of two merged rain gauge-satellite precipitation datasets. *BAMS*, **81**, 2631 – 2644.
- Hall, A. and M. Visbeck, 2002: Synchronous variability in the Southern Hemisphere atmosphere, sea ice, and ocean resulting from the annular mode. *Journal of Climate*, **15**, 3043–3057.
- Harrison, S. P., 1989: On climatological mean wind stress and wind stress curl fields over the world ocean. *J. Clim.*, **2**, 57–90.
- Holland, M. M. and M. N. Raphael, 2006: Twentieth century simulation of the Southern Hemisphere climate in coupled models. Part II: sea ice conditions and variability. *Climate Dynamics*, **26**, 229–245.
- IPCC, 2007: Summary for policy makers. In S. Solomon, D. Qin, M. Manning, Z. Chen, M. Marquis, K. B. Averyt, M. Tignor and H. L. Miller, eds., *Climate Change 2007: The Physical Science Basis. Contribution of Working Group I to the Fourth Assessment Report*

*of the Intergovernmental Panel on Climate Change*, 1–18. Cambridge University Press, Cambridge, United Kingdom, and New York, NY, USA.

Johnson, G. C., S. Mecking, B. M. Sloyan and S. E. Wijffels, 2007: Recent Bottom Water warming in the Pacific Ocean . *Journal of Climate*, **20**, 21, 5365–5375.

Josey, S., C. Kent and P. Taylor, 1999: New insights into the ocean heat budget closure problem from analysis of the SOC air-sea flux climatology . *J. Clim.*, **12**, 2856–2880.

Kushner, P. J., I. M. Held and T. L. Delworth, 2001: Southern Hemisphere atmospheric circulation response to global warming . *Journal of Climate*, **14**, 2238–2249.

Large, W. G. and G. Danabasoglu, 2006: Attribution and impacts of upper ocean biases in CCSM3 . *Journal of Climate*, **19**, 2325–2346.

Large, W. G., J. C. McWilliams and S. C. Doney, 1994: Oceanic vertical mixing: A review and a model with a nonlocal boundary layer parameterization . *Reviews of Geophysics*, **32**, 363–403.

Law, R. M., R. J. Matear and R. J. Francey, 2008: Comment on "Saturation of the Southern Ocean CO<sub>2</sub> Sink Due to Recent Climate Change". *Science*, **319**, 570a.

Le Quere, C., C. Rodenbeck, E. T. Buitenhuis, T. J. Conway, R. Langenfelds, A. Gomez, C. Labuschagne, M. Ramonet, T. Nakazawa, N. Metzl, N. P. Gillett and M. Heimann, 2007: Saturation of the Southern Ocean CO<sub>2</sub> Sink Due to Recent Climate Change. *Science*, **316**, 1735–1738.

Le Quere, C., C. Rodenbeck, E. T. Buitenhuis, T. J. Conway, R. Langenfelds, A. Gomez, C. Labuschagne, M. Ramonet, T. Nakazawa, N. Metzl, N. P. Gillett and M. Heimann, 2008: Response to Comments on "Saturation of the Southern Ocean CO<sub>2</sub> Sink Due to Recent Climate Change". *Science*, **319**, 570c.

- Lefebvre, W. and H. Goosse, 2008a: Analysis of the projected regional sea-ice changes in the Southern Ocean during the twenty-first century . *Climate Dynamics*, **30**, L07607, 59–76.
- Lefebvre, W. and H. Goosse, 2008b: Analysis of the projected changes of stratification and mixed layer depth in the Southern Ocean. *Climate Dynamic*, (submitted).
- Lovenduski, N. S., N. Gruber, S. C. Doney and I. D. Lima, 2007: Enhanced CO<sub>2</sub> outgassing in the Southern Ocean from a positive phase of the Southern Annular Mode. *Global Biogeochemical Cycles*, **21**, GB2026.
- Marshall, G. J., P. A. Stott, J. Turner, W. M. Connolley, J. C. King and T. A. Lachlan-Cope, 2004: Causes of exceptional atmospheric circulation changes in the Southern Hemisphere . *Geophysical Research Letters*, **31**, doi:10.1029/2004GL019952.
- Meehl, G. A., C. Covey, T. Delworth, M. Latif, B. McAvaney, J. F. B. Mitchell, R. J. Stouffer and K. E. Taylor, 2007: The WCRP CMIP3 multimodel dataset: A new era in climate change research . *Bulletin of the American Meteorological Society*, **88**, 9, 1383–1394.
- Meehl, G. A., C. Covey, B. McAvaney, M. Latif and R. J. Stouffer, 2005: Overview of the Coupled Model Intercomparison Project. *Bulletin of the American Meteorological Society*, **86**, 1, 89–93.
- Mellor, G. and L. Kantha, 1989: An ice-ocean coupled model. *Journal of Geophysical Research*, **94**, 10 937–10 954.
- Meredith, M. and A. Hogg, 2006: Circumpolar response of Southern Ocean eddy activity to a change in the Southern Annular Mode. *Geophysical Research Letters*, **33**, doi:10.1029/2006GL026499.

- Nakano, H. and N. Sugimotohara, 2002: Effects of bottom boundary layer parameterization on reproducing deep and bottom waters in a world ocean model . *Journal of Physical Oceanography*, **32**, 1209–1227.
- Nakicenovic, N., R. Swart and (Eds.), 2000: IPCC Special Report on Emissions Scenarios. Cambridge University Press, Cambridge, 292 UK. .
- Noh, Y. and H. J. Kim, 1999: Simulations of temperature and turbulence structure of the oceanic boundary layer with the improved near-surface process. *Journal of Geophysical Research*, **104**, 15 621–15 634.
- Oke, P. R. and M. H. England, 2004: Oceanic response to changes in the latitude of the Southern Hemisphere subpolar westerly winds . *Journal of Climate*, **17**, 1040–1054.
- Olbers, D., D. Borowski, C. Volker and J.-O. Wolff, 2004: The dynamical balance, circulation and transport of the Antarctic Circumpolar Current . *Antarctic Science*, **16**, doi: 10.1017/S095410200400.
- Pacanowski, R. C. and S. G. H. Philander, 1981: Parameterisation of vertical mixing in numerical models of tropical oceans . *Journal of Physical Oceanography*, **11**, 11, 1443–1451.
- Parkinson, C. L., K. Y. Vinnikov and D. J. Cavalieri, 2006: Evaluation of the simulation of the annual cycle of Arctic and Antarctic sea ice coverages by 11 major global climate models . *Journal of Geophysical Research*, **111**, C07012, doi:10.1029/2005JC003408.
- Quartly, G. D., E. Kyte, A. A. Srokosz and M. N. Tsimplis, 2007: An intercomparison of global oceanic precipitation climatologies. *JGR*, **112**, doi:10.1029/2006JD007810.
- Randall, D. A., R. A. Wood, S. Bony, R. Colman, T. Fichefet, J. Fyfe, V. Kattsov, A. Pitman, J. Shukla, J. Srinivasan, R. J. Stouffer, A. Sumi and K. E. Taylor, 2007: Climate models and their evaluation. In S. Solomon, D. Qin, M. Manning, Z. Chen,

- M. Marquis, K. B. Averyt, M. Tignor and H. L. Miller, eds., *Climate Change 2007: The physical science basis. Contribution of Working Group I to the Fourth Assessment Report of the Intergovernmental Panel on Climate Change*, 589–662. Cambridge University Press, Cambridge, United Kingdom, and New York, NY, USA.
- Ridgway, K. R., J. R. Dunn and J. L. Wilkin, 2002: Ocean interpolation by four-dimensional least squares - Application to the waters around Australia . *J. Atmos. Ocean. Tech.*, **19**, 1357–1375.
- Rintoul, S. R., 2007: Rapid freshening of Antarctic Bottom Water formed in the Indian and Pacific oceans . *Geophysical Research Letters*, **34**, L06606, doi:10.1029/2006GL028550.
- Rintoul, S. R., C. W. Hughes and D. Olbers, 2001: Antarctic Circumpolar Current system. In G. Siedler, J. Church and J. Gould, eds., *Ocean circulation and climate*, 271–302. Academic Press, New York.
- Roemmich, D., J. Gilson, R. Davis, P. Sutton, S. Wijffels and S. Riser, 2007: Decadal spinup of the South Pacific subtropical gyre . *Journal of Physical Oceanography*, **37**, 162–173.
- Russell, G., J. Miller and D. Rind, 1995: A coupled atmosphere-ocean model for transient climate change studies. *Atmos. Ocean*, **33**, 683–730.
- Russell, G. L., J. R. Miller, D. Rind, R. A. Ruedy, G. A. Schmidt and S. Sheth, 2000: Comparison of model and observed regional temperature changes during the past 40 years. *Journal of Geophysical Research*, **105**, 14,891–14,898.
- Russell, J. L., K. W. Dixon, A. Gnanadesikan, R. J. Stouffer and J. R. Toggweiler, 2006a: The Southern Hemisphere westerlies in a warming world: Propping open the door to the deep ocean. *Journal of Climate*, **19**, 24, 6382–6390.

- Russell, J. L., R. J. Stouffer and K. W. Dixon, 2006b: Intercomparison of the Southern Ocean circulations in IPCC coupled model control simulations. *Journal of Climate*, **19**, 18, 4560–4575.
- Sabine, C., R. Feely, N. Gruber, R. Key, K. Lee, J. Bullister, R. Wanninkhof, C. Wong, D. Wallace, B. Tilbrook, F. Millero, T. Peng, A. Kozyr, T. Ono and A. F. Rios, 2004: The Oceanic Sink for Anthropogenic  $CO_2$  . *Science*, **305**, 5682, 367–371.
- Saenko, O., J. Fyfe and M. England, 2005: On the response of the oceanic wind-driven circulation to atmospheric  $CO_2$  increase. *Climate Dynamics*, **25**, 415–426.
- Santoso, A., M. H. England and A. C. Hirst, 2006: Circumpolar Deep Water Circulation and Variability in a Coupled Climate Model. *Journal of Physical Oceanography*, **36**, 1523–1552.
- Sen Gupta, A. and M. England, 2006: Coupled Ocean-Atmosphere-Ice Response to variations in the Southern Annular Mode . *Journal of Climate*, **19**, 18, 4457–4486.
- Serreze, M. C., M. M. Holland and J. Stroeve, 2007: Perspectives on the Arctic’s shrinking sea-ice cover . *Science*, **315**, 1533–1536.
- Simmonds, I. and K. Keay, 2000: Variability of Southern Hemisphere extratropical cyclone behavior 1958 - 97. *Journal of Climate*, **13**, 550288.
- Simmonds, I., K. Keay and E.-P. Lim, 2003: Synoptic activity in the seas around Antarctica. *Monthly Weather Review*, **131**, 272288.
- Son, S.-W., L. M. Polvani, D. W. Waugh, H. Akiyoshi, R. Garcia, D. Kinnison, S. Pawson, E. Rozanov, T. G. Shepherd and K. Shibata, 2008: The Impact of Stratospheric Ozone Recovery on the Southern Hemisphere Westerly Jet . *Science*, **320**, 1486–1489.
- Stammerjohn, S. E., D. G. Martinson, R. C. Smith, X. Yuan and D. Rind, 2008: Trends in Antarctic annual sea-ice retreat and advance and their relation to El Niño-Southern

- Oscillation and Southern Annular Mode variability . *Journal of Geophysical Research*, **113**, C03S90, doi:10.1029/2007JC004269.
- Taschetto, A. S. and I. Wainer, 2008: Reproducibility of South American Precipitation due to Subtropical South Atlantic SSTs. *Journal of Climate*, **21**, 2835–2851.
- Taylor, P. K., 2000: Intercomparison and validation of ocean-atmosphere energy flux fields. 303pp.
- Thompson, D. W. J. and S. Solomon, 2002: Interpretation of recent Southern Hemisphere climate change . *Science*, **296**, 895–899.
- Thompson, D. W. J. and J. M. Wallace, 2000: Annular modes in the extratropical circulation. Part I: month-to-month variability . *Journal of Climate*, **13**, 1000–1016.
- Thompson, D. W. J., J. M. Wallace and G. C. Hegerl, 2000: Annular modes in the extratropical circulation. Part II: Trends . *Journal of Climate*, **13**, 1018–1036.
- Toggweiler, J. R. and J. Russell, 2008: Ocean circulation in a warming climate. *Nature*, **451**, 286–288.
- Uppala, S. M., P. W. Kallberg, A. J. Simmons, U. Andrae, V. da Costa Bechtold, M. Fiorino, J. K. Gibson, J. Haseler, A. Hernandez, G. A. Kelly, X. Li, K. Onogi, S. Saarinen, N. Sokka, R. P. Allan, E. Andersson, K. Arpe, M. A. Balmaseda, A. C. Beljaars, L. van de Berg, J. Bidlot, N. Bormann, S. Caires, F. Chevallier, A. Dethof, M. Dragosavac, M. Fisher, M. Fuentes, S. Hagemann, E. Holm, B. J. Hoskins, L. Isaksen, P. A. Janssen, R. Jenne, A. P. McNally, J. F. Mahfouf, J. J. Morcrette, N. A. Rayner, R. W. Saunders, P. Simon, A. Sterl, K. E. Trenberth, A. Untch, D. Vasiljevic, P. Viterbo and J. Woollen, 2005: The ERA-40 re-analysis. *QJRM*S, **131**, 2961–3012. Doi:10.1256/qj.04.176.
- Visbeck, M., J. Marshall, T. Haine and M. Spall, 1997: Specification of eddy transfer



- coefficients in coarse resolution ocean circulation models . *Journal of Physical Oceanography*, **27**, 381–402.
- Wainer, I., A. S. Taschetto, B. Otto-Bliesner and E. Brady, 2004: A numerical study of the impact of greenhouse gases on the South Atlantic Ocean climatology. *Clim. Change*.
- Xie, P. and P. A. Arkin, 1997: Global Precipitation: A 17-year monthly analysis based on gauge observations, satellite estimates, and numerical model outputs. *Bull. Am. Meteorol. Soc.*, **78**, 2539–2558.
- Yin, J. H., 2005: A consistent poleward shift of the storm tracks in simulations of 21st century climate . *Geophysical Research Letters*, **32**, L18701, doi:10.1029/2005GL023684.
- Yu, Y., B. Wang, T. Zhou, H. Liu and X. Zhang, ????: Known biases in IAP/LASG FGOALS\_g1.0 model and the recent improvements. URL [http://www-pcmdi.llnl.gov/ipcc/model\\_documentation/more\\_info\\_iap\\_fggoals.pdf](http://www-pcmdi.llnl.gov/ipcc/model_documentation/more_info_iap_fggoals.pdf).
- Zickfeld, K., J. C. Fyfe, M. Eby and A. J. Weaver, 2008: Comment on "Saturation of the Southern Ocean CO<sub>2</sub> Sink Due to Recent Climate Change". *Science*, **319**, 570b.

## List of Figures

- 1 Model drift calculated as the linear trend in zonally averaged temperature at each grid point over the 100 year period coincident with the 21<sup>st</sup> century (colour contours). Both individual models and the multi-model mean are shown. Superimposed is the ratio of the model drift to the projected change (20C to 21C), such that a value of one implies that the magnitude of the drift is of equal magnitude to the projected change. . . . . 49
- 2 Multi-model (20C) mean (left), standard deviation (second column), difference from observation (third column) and projected change (21C-20C, right) of (a-d) Wind stress [ $Nm^{-2}$ ], (e-h) wind stress curl [ $Nm^{-1}$ ], (i-l) precipitation, [ $mm d^{-1}$ ] (m-p) latent heat flux [ $Wm^{-2}$ ], (q-t) sensible heat flux [ $Wm^{-2}$ ], and (u-x) net heat flux [ $Wm^{-2}$ ]. Positive heat fluxes indicate gain to the ocean. Observations of wind-stress and wind-stress curl based on the ECMWF Reanalysis ERA40 reanalysis (1979 to 2001 Uppala *et al.*, 2005). Precipitation observations based on CMAP gridded dataset (1979-2006 Xie and Arkin, 1997). Heat fluxes based on the SOC gridded observations (Josey *et al.*, 1999). . . . . 50
- 3 Zonally-averaged wind-stress [ $Nm^{-2}$ ] (a), wind-stress curl [ $Nm^{-1}$ ] (b), precipitation [ $mm d^{-1}$ ] (c), latent heat flux [ $Wm^{-2}$ ] (d), sensible heat flux [ $Wm^{-2}$ ] (e), net radiative flux [ $Wm^{-2}$ ] (f), and net heat flux [ $Wm^{-2}$ ] (g) from the multi-model ensemble for 20C and 21C. Red (blue) areas represent a strengthening (weakening) of the variable from 20C to 21C. Yellow line represents ERA40 results. Green line: (c) CMAP and (d-f) SOC. Grey lines indicate 20C zonal averages for the individual models. . . . . 51

- 4 Scatter plots for (a) zonally averaged wind-stress maximum position ( $\tau_P$ ) versus zonally averaged wind-stress maximum strength ( $\tau_S$ ) [ $Nm^{-2}$ ], (b)  $\Delta\tau_P$  versus  $\Delta\tau_S$ , (c)  $\tau_P$  versus position of ACC core ( $ACC_P$ , calculated from zonally averaged depth integrated zonal velocity), (d)  $\tau_S$  versus ACC core strength ( $ACC_S$ ) [Sv], (e)  $\Delta\tau_P$  versus  $\Delta ACC_P$ , (f)  $\Delta\tau_S$  versus  $\Delta ACC_S$ , (g)  $\nabla \times \tau_P$  versus position of minimum zonally averaged barotropic stream function (STF), (h)  $\Delta(\nabla \times \tau_P)$  versus  $\Delta STF$ . Where either ordinate or abscissa values are missing for a given model the value for the available variable is plotted along the side of the panel. Key: 1: Obs, 2: CGCM3.1(T47), 3: CGCM3.1(T63), 4: CNRM-CM3, 5: CSIRO3.0, 6: CSIRO3.5, 7: GFDL-CM2.0, 8: GFDL-CM2.1, 9: GISS-AOM, 10: GISS-ER, 11: FGOALS-g1.0, 12: ECHAM4, 13: INM-CM3.0, 14: IPSL-CM4, 15: MIROC3.2(hires), 16: MIROC3.2(medres), 17: ECHO-G, 18: ECHAM5, 19: MRI-CGCM2.3.2, 20: CCSM3.0, 21: PCM, 22: UKMO-HadCM3. Models where ozone hole recovery over the 21st century is simulated are highlighted with a 'x' (based on information from Son *et al.*, 2008); those where information regarding ozone recovery is unavailable are highlighted with a '-'; all other models do not simulate a recovery. Correlation coefficients (r), p-values (p) and a best fit linear regression lines are also shown. 52
- 5 Multi-model mean bias ( $20C$ -observations; a,b), standard deviation (c,d) and difference ( $21C$ - $20C$ ; e,f) for temperature [K] (left) and salinity [ppt] (right). Mottled areas are not significant at 90% level. Bottom panels show zonally averaged temperature (g) and salinity (h) for individual models (grey- $20C$ , pink- $21C$ ), the multi model means (black- $20C$ , red  $21C$ ), and observations (dashed). The side panel depicts the zonally averaged Ekman transport  $[-\tau/f]$ , with northward transport at higher latitudes. Line contours in panel (e) shows the multi-model mean 20C maximum mixed layer depths . . . . . 53

- 6 Maximum mixed layer depth [m] for  $20C$  for individual models (upper panels), multi-model and observations (lower panels). Superimposed is  $21^{st}$  century change in MLD (contour interval 50m, dashed lines indicate shoaling. Also shown is the inter model standard deviation (bottom middle panel, colour contours) with the  $20C$  MLD superimposed for reference. Buoyancy,  $B$ , used for MLD criteria, is calculated as  $B = g(1 - \sigma_{surface}/\sigma_{mld})$ , where  $\sigma$  is the potential density (see Griffies *et al.*, 2008). All colour ranges are the same except for the standard deviation panel. . . . . 54
- 7 Mid-latitudes mixed layer depth frequency distribution, for domain  $30^{\circ}$ - $60^{\circ}$ S, (except between  $160^{\circ}$ - $300^{\circ}$ E where  $30^{\circ}$ - $65^{\circ}$ S is used) showing the area within the domain with MLD of a given depth (in bins of 20m) [units  $m^2$ ]. Grey line -observation, black bars- model. Blue (red) shading indicates a 21st century decrease (increase) in the area associated with a given MLD range. . . . . 55
- 8 Barotropic stream function for the multi-model mean (colour contours, white labels) and observations (line contours, black labels), derived from the University of Maryland's Simple Ocean Data Assimilation Reanalysis (SODA version 2.0.2-3) zonal velocities. Positive stream-line spacing 25Sv, negative spacing 10Sv. Stream functions have been adjusted so the zero contour passes through the northern limit of the Drake Passage . . . . . 56
- 9 Lateral, depth averaged circulation and heat content changes. Colour contours show the projected change in the depth integrated heat content ( $21C$ - $20C$ ; J/ $m^2$ ). Superimposed are (i) Mean barotropic stream function for  $20C$  (black) and  $21C$  (green, only streamlines indicative of subtropical gyre positions are shown) and (ii) position of ACC maximum for  $20C$  and  $21C$  (red/blue shading between lines indicates poleward/equatorward movement of ACC axis over the period). Dotted line indicates mean position of the observed ACC. . . . . 57
- 10 As Fig. 9 for the multi-model mean. . . . . 58

- 11    Strength [ $Sv$ ] of the EAC, Brazil and Agulhas western boundary currents by latitude. WBC strength shown as depth integrated velocity, calculated as the gradient of the barotropic stream function. Red (black) areas indicate locations when future strengths are increased (decreased) with respect to present day. Cores strengths are defined as the average flow, where flow exceeds 80% of the maximum value at a given latitude and near to the continental margin. For the EAC the flow is simply the southward depth integrated velocity, while for the Brazil and Agulhas currents the flow is the depth integrated component of velocity in the south westward direction. . . . . 59
- 12    Projected change in MOC ( $21C-21C$ , colour maps). Only differences that are significant above the 95% level are displayed. The significance level is determined by two tailed t-test. The  $20C$  mean state of MOC is superimposed. Bottom left panel shows multi-model mean of  $20C$  MOC [solid contours for positive MOC (4Sv interval), dashed for negative (1Sv interval)] and projected changes (colour map). Bottom right panel shows the multi-model standard deviation for both the  $20C$  mean states (contours with 1Sv interval) and projected changes (colour map). . . . . 60

- 13 Projected differences in the transport [ $Sv$ ] of the Southern Ocean overturning cells for individual models (circles). Red circles indicate that the data have been drift corrected while black circles are based on uncorrected data. Horizontal error bars indicate the corresponding 95% confidence interval with filled circles indicating significant difference from zero. The multi-model mean differences (corrected and uncorrected) are indicated by the corresponding dashed vertical lines with the grey region indicating the 95% confidence interval for the red (drift corrected) vertical line. The 20C mean values of each model overturning cell are shown on the left of each panel with the multi-model mean values shown in bold at the bottom. Mean values that fall within 95% confidence interval of the multi-model mean are also shown in bold while the values that fall in the upper (lower) tail of the 95% interval are shown in grey (black). Note that the pre-industrial run of ECHAM5 is not available for estimating the drift. Its uncorrected values are shown nonetheless. . . . . 61
- 14 Projected change in the zonally averaged potential temperature (colour contours). Superimposed contours indicate the changes that would result from a southward shift of the  $20C$  temperature distribution by  $1^\circ$  latitude. Contour interval  $0.2^\circ C$ , with zero contour in grey. Black solid (dashed) contours indicate positive (negative) changes with an absolute maximum value of  $1^\circ C$ . . 62
- 15 As Fig. 14 for salinity. Yellow contour is a salinity contour representative of the salinity minimum, associated with the pathway of intermediate water. Line contour interval is 0.01 psu with an absolute maximum contour value of 0.1 psu . . . . . 63
- 16 As for figs. 14 and 15 for multi-model mean global and individual basin zonal averages. Upper panels show the anomalous ( $21C-20C$ ) Ekman related transport of heat (left) and salt (right). Right panel also shows the anomalous salt flux due to precipitation (dashed curve), using a 50m surface layer. . . . . 64

17	Projected change in potential density over the 21st century (colour contours). Superimposed are <i>20C</i> (black) and <i>21C</i> (red) isopycnals. Mottling indicates regions where salinity is playing a large role (>50% heavy mottling, >25% light mottling) in controlling the density change. . . . .	65
18	Winter (top) and summer (bottom) <i>20C</i> sea-ice concentration (% cover) for observation (left) and multi-model mean (right; excluding <i>FGOALS-g1.0</i> ). Su- perimposed contours show the percentage change in sea-ice concentration be- tween <i>20C</i> and <i>21C</i> (contour interval 5%, dashed contours denote reduction in sea-ice). . . . .	66
19	Schematic showing the robust changes in the SH extratropics. . . . .	67

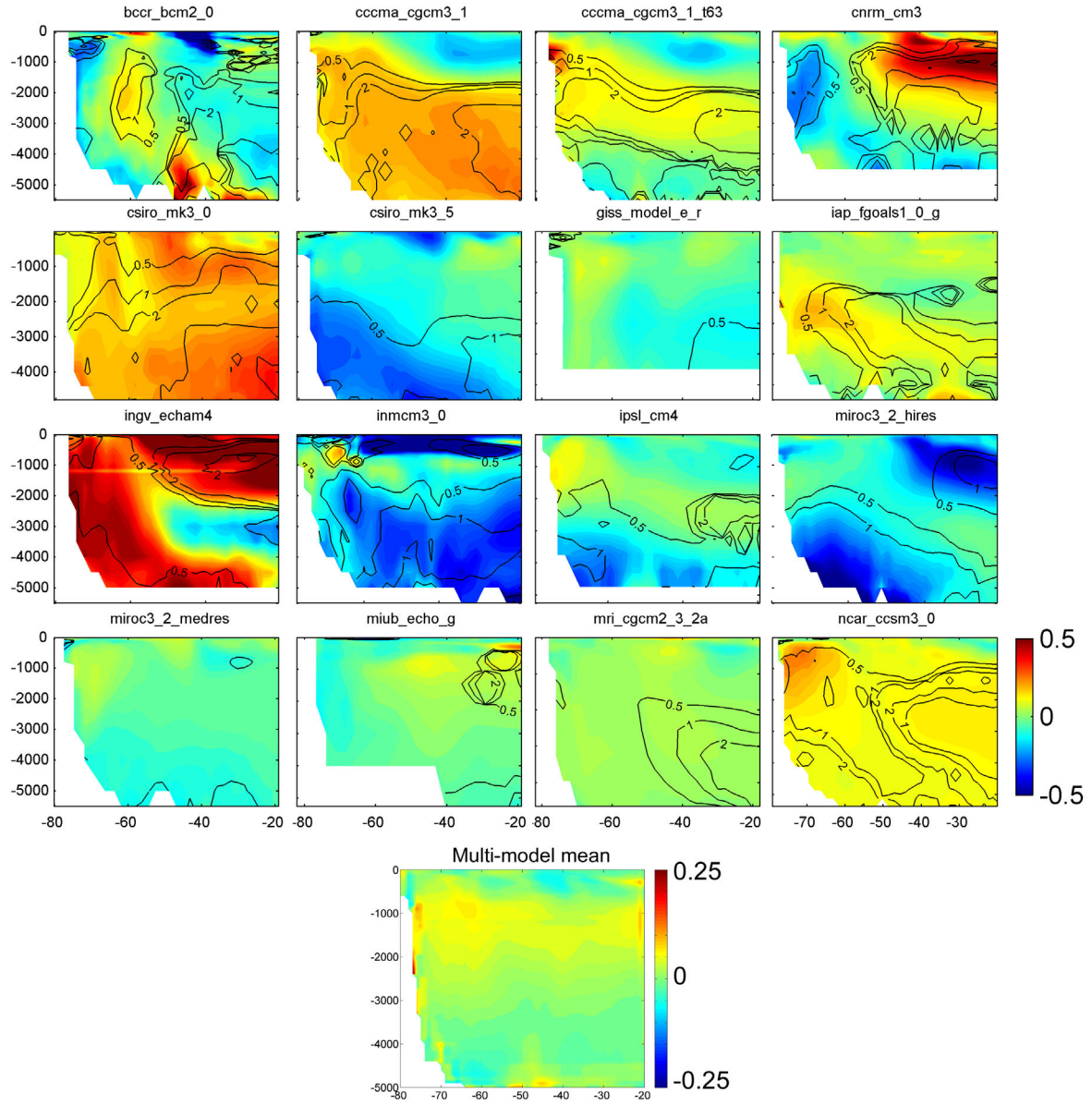


**Figure 1.** Model drift calculated as the linear trend in zonally averaged temperature at each grid point over the 100 year period coincident with the 21<sup>st</sup> century (colour contours). Both individual models and the multi-model mean are shown. Superimposed is the ratio of the model drift to the projected change (20C to 21C), such that a value of one implies that the magnitude of the drift is of equal magnitude to the projected change.



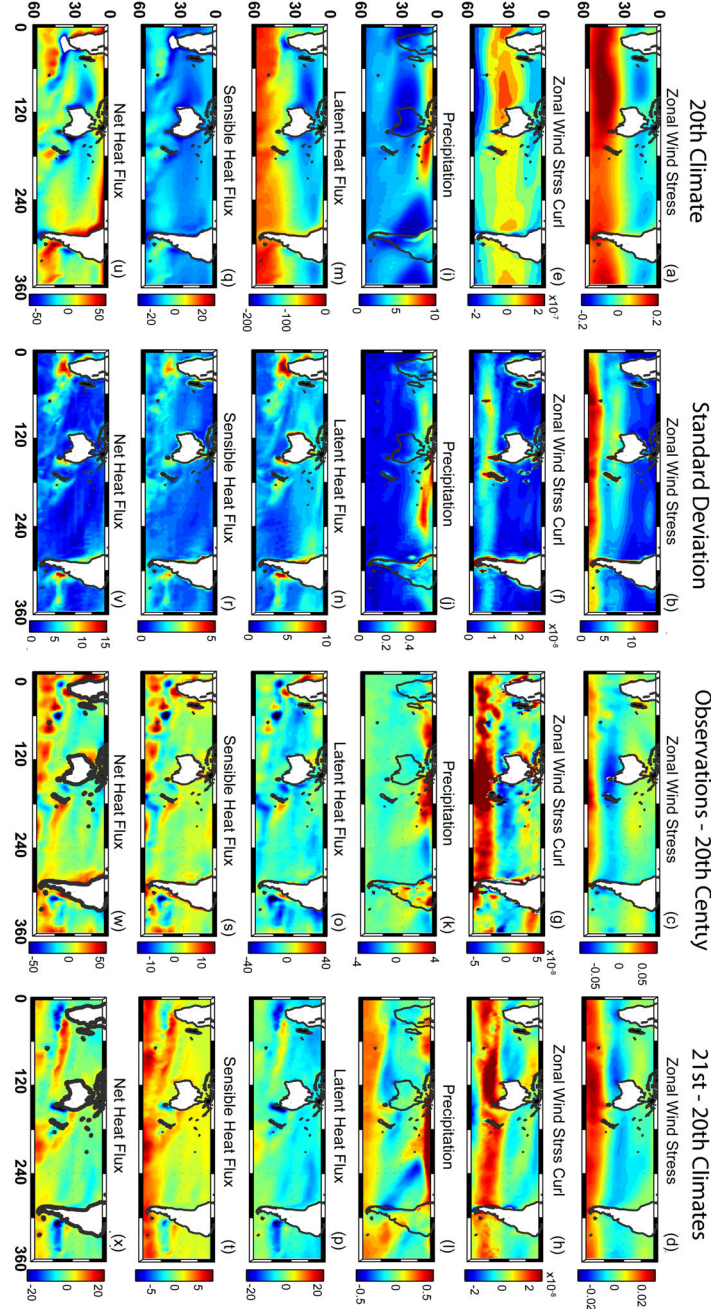


**Figure 2.** Multi-model (20C) mean (left), standard deviation (second column), difference from observation (third column) and projected change (21C-20C, right) of (a-d) Wind stress [ $Nm^{-2}$ ], (e-h) wind stress curl [ $Nm^{-1}$ ], (i-l) precipitation, [ $mmd^{-1}$ ] (m-p) latent heat flux [ $Wm^{-2}$ ], (q-t) sensible heat flux [ $Wm^{-2}$ ], and (u-x) net heat flux [ $Wm^{-2}$ ]. Positive heat fluxes indicate gain to the ocean. Observations of wind-stress and wind-stress curl based on the ECMWF Reanalysis ERA40 reanalysis (1979 to 2001 Uppala *et al.*, 2005). Precipitation observations based on CMAP gridded dataset (1979-2006 Xie and Arkin, 1997). Heat fluxes based on the SOC gridded observations (Josey *et al.*, 1999).

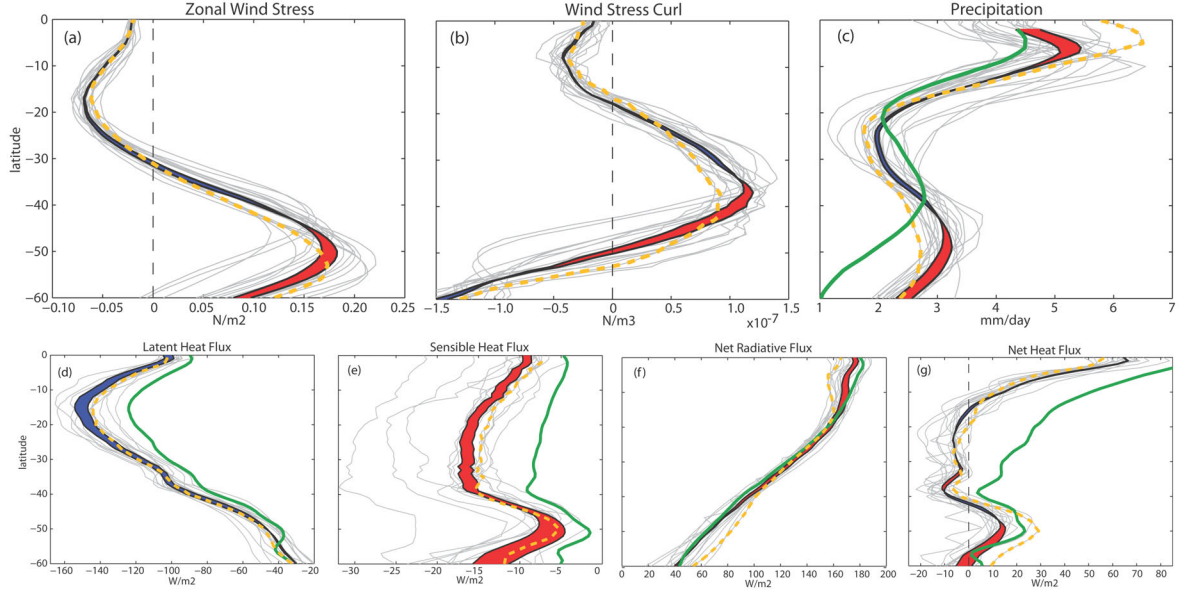


**Figure 3.** Zonally-averaged wind-stress [ $Nm^{-2}$ ] (a), wind-stress curl [ $Nm^{-1}$ ] (b), precipitation [ $mm d^{-1}$ ] (c), latent heat flux [ $Wm^{-2}$ ] (d), sensible heat flux [ $Wm^{-2}$ ] (e), net radiative flux [ $Wm^{-2}$ ] (f), and net heat flux [ $Wm^{-2}$ ] (g) from the multi-model ensemble for *20C* and *21C*. Red (blue) areas represent a strengthening (weakening) of the variable from *20C* to *21C*. Yellow line represents ERA40 results. Green line: (c) CMAP and (d-f) SOC. Grey lines indicate *20C* zonal averages for the individual models.

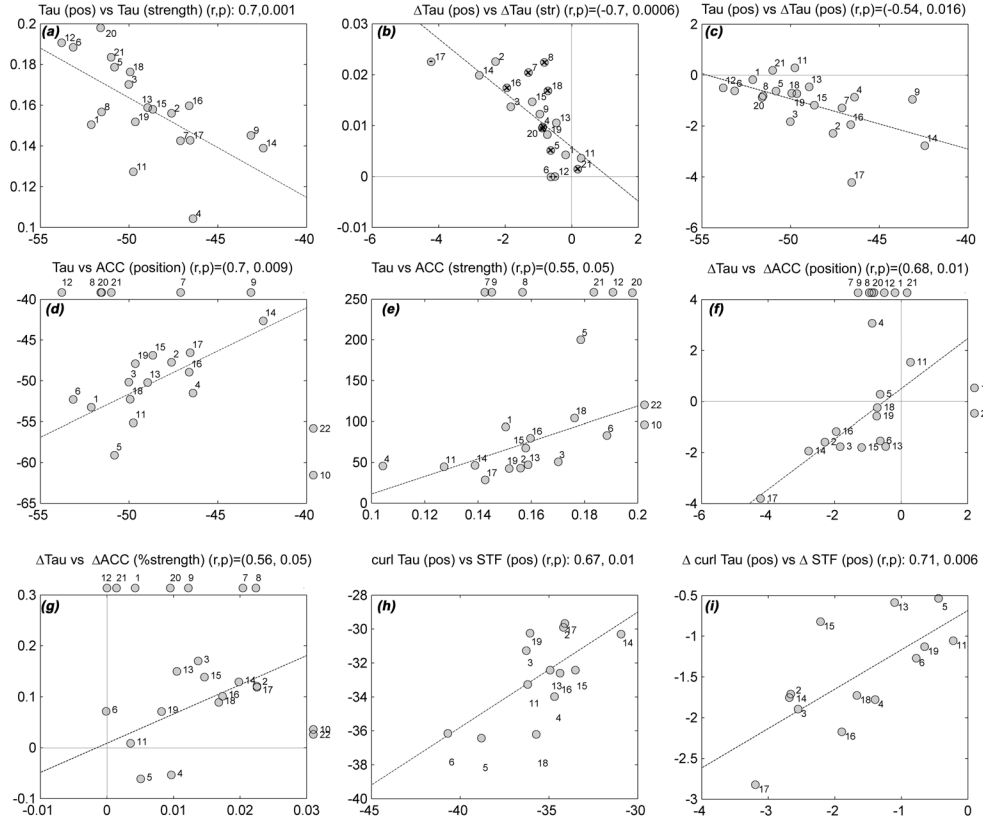


**Figure 4.** Scatter plots for (a) zonally averaged wind-stress maximum position ( $\tau_P$ ) versus zonally averaged wind-stress maximum strength ( $\tau_S$ ) [ $Nm^{-2}$ ], (b)  $\Delta\tau_P$  versus  $\Delta\tau_S$ , (c)  $\tau_P$  versus position of ACC core ( $ACC_P$ , calculated from zonally averaged depth integrated zonal velocity), (d)  $\tau_S$  versus ACC core strength ( $ACC_S$ ) [Sv], (e)  $\Delta\tau_P$  versus  $\Delta ACC_P$ , (f)  $\Delta\tau_S$  versus  $\Delta ACC_S$ , (g)  $\nabla \times \tau_P$  versus position of minimum zonally averaged barotropic stream function (STF), (h)  $\Delta(\nabla \times \tau_P)$  versus  $\Delta STF$ . Where either ordinate or abscissa values are missing for a given model the value for the available variable is plotted along the side of the panel. Key: 1: Obs, 2: CGCM3.1(T47), 3: CGCM3.1(T63), 4: CNRM-CM3, 5: CSIRO3.0, 6: CSIRO3.5, 7: GFDL-CM2.0, 8: GFDL-CM2.1, 9: GISS-AOM, 10: GISS-ER, 11: FGOALS-g1.0, 12: ECHAM4, 13: INM-CM3.0, 14: IPSL-CM4, 15: MIROC3.2(hires), 16: MIROC3.2(medres), 17: ECHO-G, 18: ECHAM5, 19: MRI-CGCM2.3.2, 20: CCSM3.0, 21: PCM, 22: UKMO-HadCM3. Models where ozone hole recovery over the 21st century is simulated are highlighted with a 'x' (based on information from Son *et al.*, 2008); those where information regarding ozone recovery is unavailable are highlighted with a '-'; all other models do not simulate a recovery. Correlation coefficients ( $r$ ), p-values ( $p$ ) and a best fit linear regression lines are also shown.

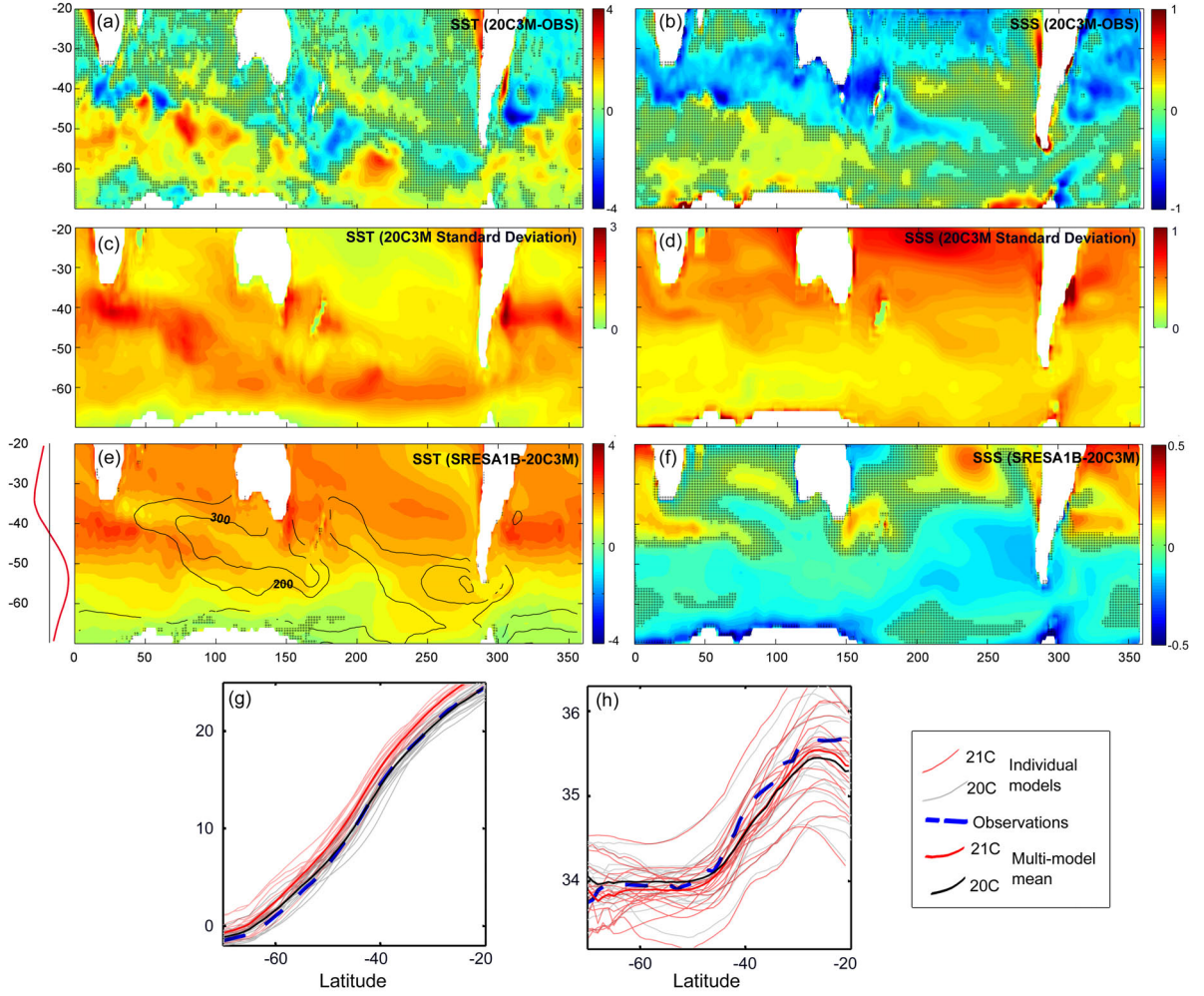


**Figure 5.** Multi-model mean bias ( $20C$ -observations; a,b), standard deviation (c,d) and difference ( $21C$ - $20C$ ; e,f) for temperature [K] (left) and salinity [ppt] (right). Mottled areas are not significant at 90% level. Bottom panels show zonally averaged temperature (g) and salinity (h) for individual models (grey-  $20C$ , pink-  $21C$ ), the multi model means (black-  $20C$ , red  $21C$ ), and observations (dashed). The side panel depicts the zonally averaged Ekman transport  $[-\tau/f]$ , with northward transport at higher latitudes. Line contours in panel (e) shows the multi-model mean  $20C$  maximum mixed layer depths



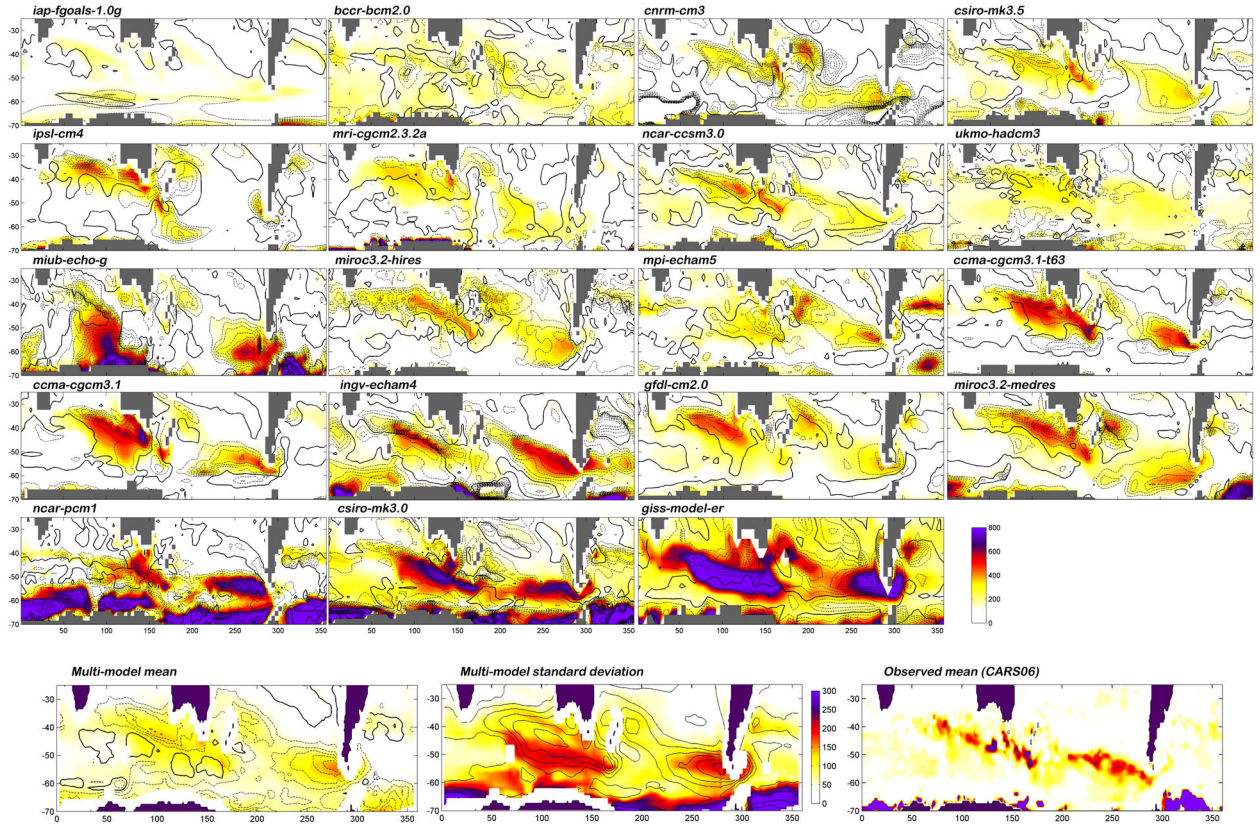


**Figure 6.** Maximum mixed layer depth [m] for  $20C$  for individual models (upper panels), multi-model and observations (lower panels). Superimposed is  $21^{st}$  century change in MLD (contour interval 50m, dashed lines indicate shoaling). Also shown is the inter model standard deviation (bottom middle panel, colour contours) with the  $20C$  MLD superimposed for reference. Buoyancy,  $B$ , used for MLD criteria, is calculated as  $B = g(1 - \sigma_{surface}/\sigma_{mld})$ , where  $\sigma$  is the potential density (see Griffies *et al.*, 2008). All colour ranges are the same except for the standard deviation panel.

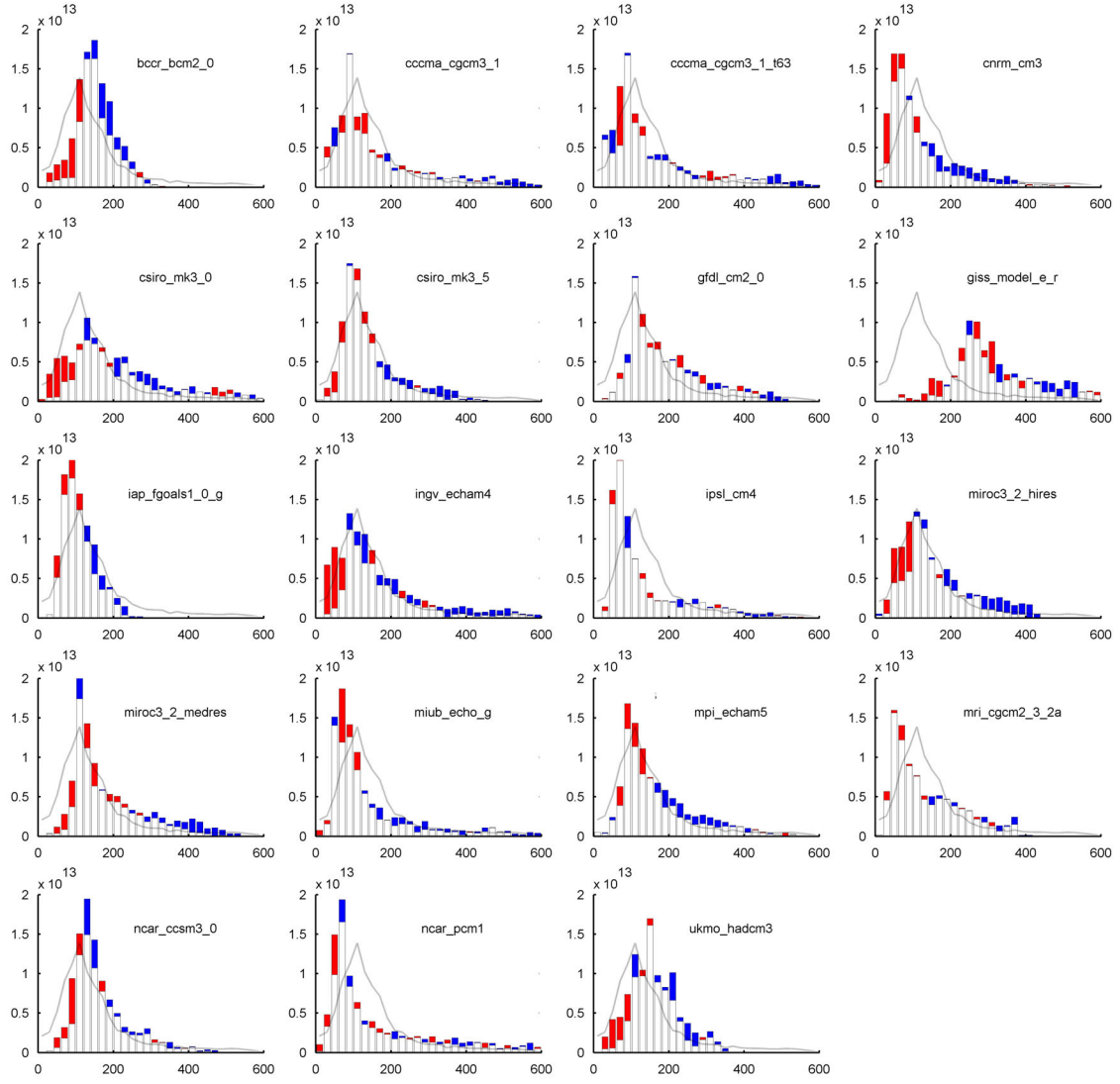


**Figure 7.** Mid-latitudes mixed layer depth frequency distribution, for domain  $30^{\circ}$ - $60^{\circ}$ S, (except between  $160^{\circ}$ - $300^{\circ}$ E where  $30^{\circ}$ - $65^{\circ}$ S is used) showing the area within the domain with MLD of a given depth (in bins of 20m) [units  $\text{m}^2$ ]. Grey line -observation, black bars-model. Blue (red) shading indicates a 21st century decrease (increase) in the area associated with a given MLD range.

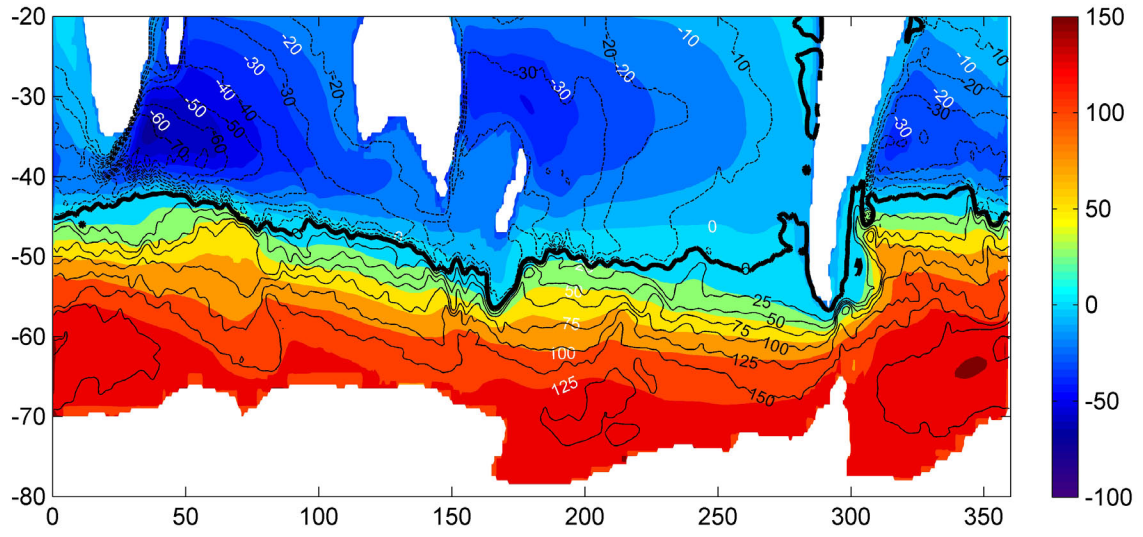


**Figure 8.** Barotropic stream function for the multi-model mean (colour contours, white labels) and observations (line contours, black labels), derived from the University of Maryland’s Simple Ocean Data Assimilation Reanalysis (SODA version 2.0.2-3) zonal velocities. Positive stream-line spacing 25Sv, negative spacing 10Sv. Stream functions have been adjusted so the zero contour passes through the northern limit of the Drake Passage



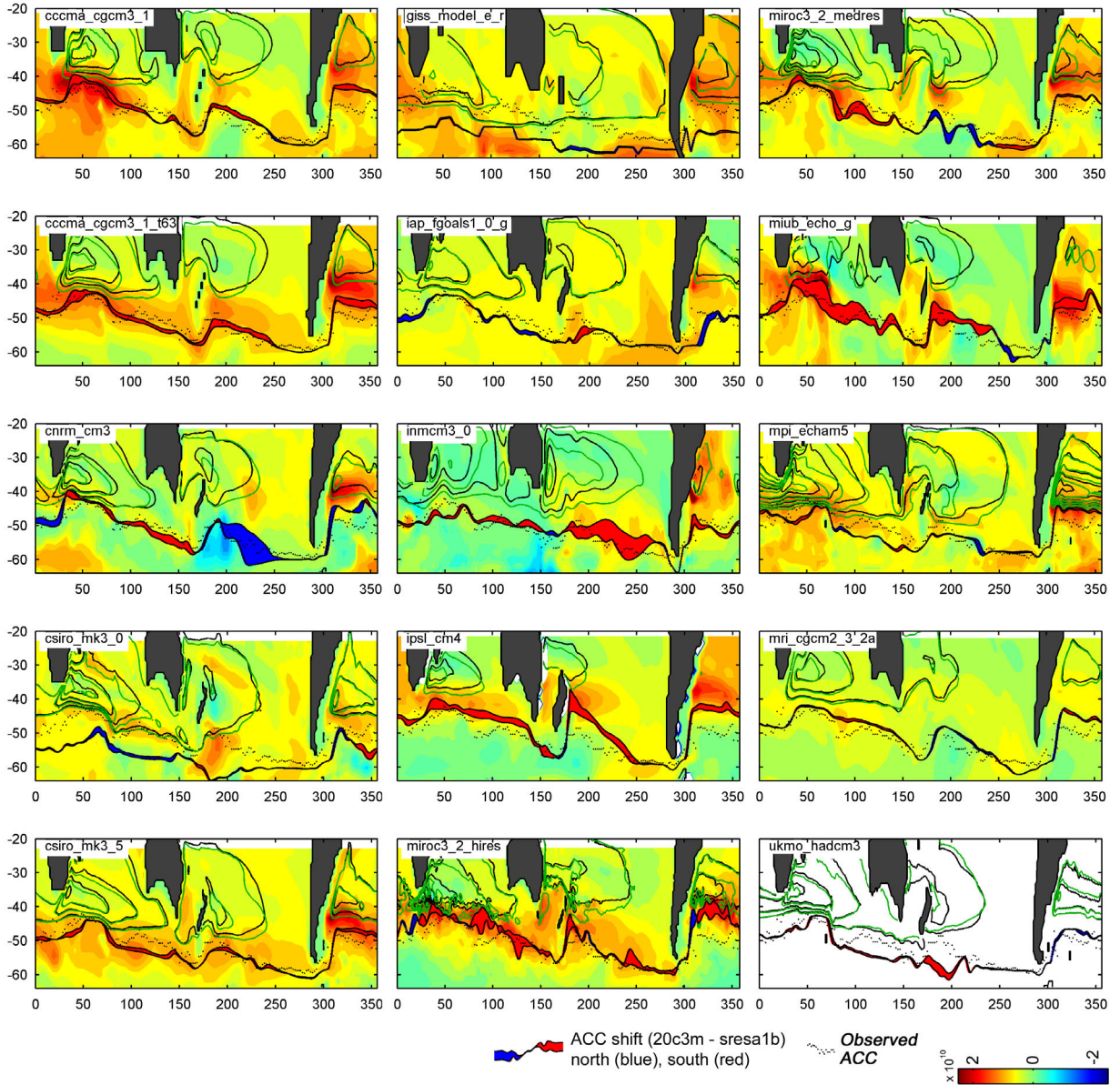


**Figure 9.** Lateral, depth averaged circulation and heat content changes. Colour contours show the projected change in the depth integrated heat content ( $21C-20C$ ;  $J/m^2$ ). Superimposed are (i) Mean barotropic stream function for  $20C$  (black) and  $21C$  (green, only streamlines indicative of subtropical gyre positions are shown) and (ii) position of ACC maximum for  $20C$  and  $21C$  (red/blue shading between lines indicates poleward/equatorward movement of ACC axis over the period). Dotted line indicates mean position of the observed ACC.



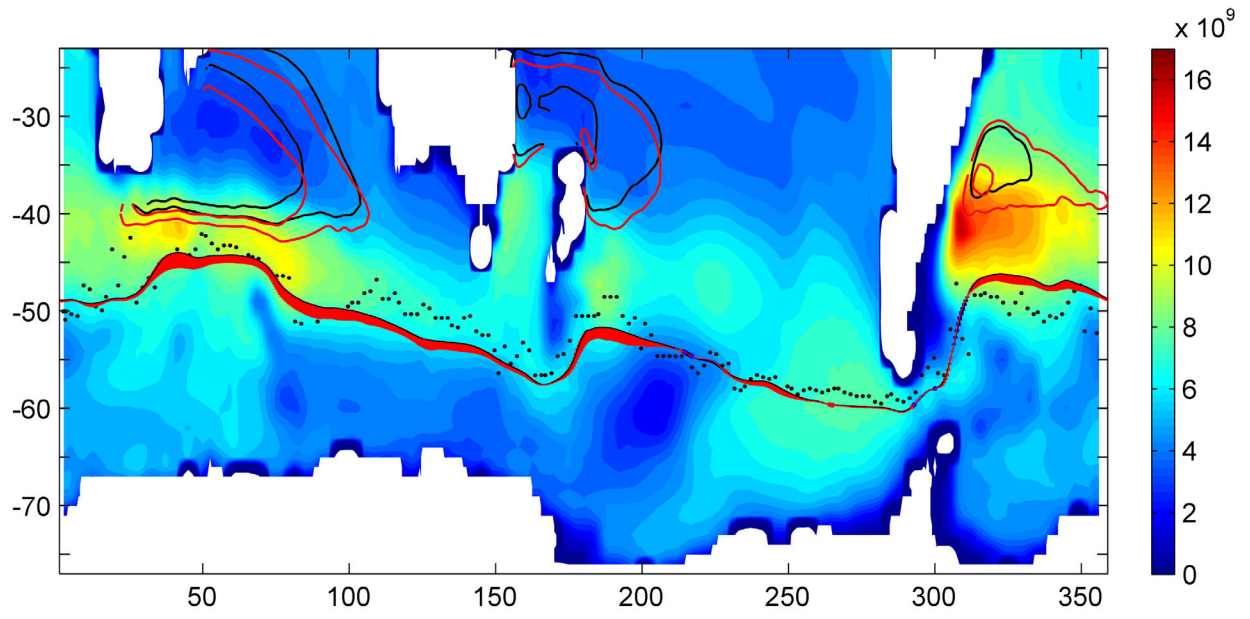


**Figure 10.** As Fig. 9 for the multi-model mean.

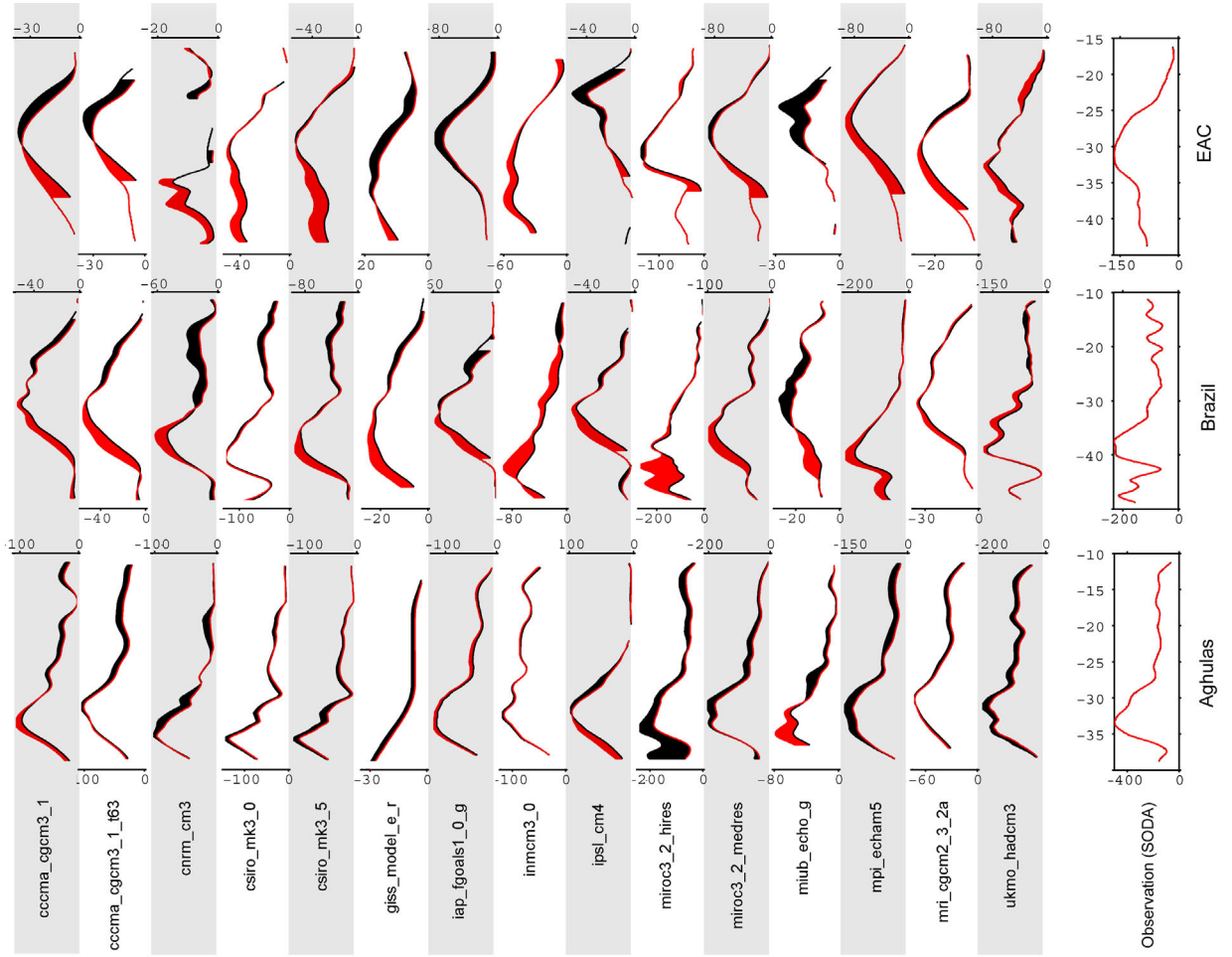


**Figure 11.** Strength [ $Sv$ ] of the EAC, Brazil and Agulhas western boundary currents by latitude. WBC strength shown as depth integrated velocity, calculated as the gradient of the barotropic stream function. Red (black) areas indicate locations when future strengths are increased (decreased) with respect to present day. Cores strengths are defined as the average flow, where flow exceeds 80% of the maximum value at a given latitude and near to the continental margin. For the EAC the flow is simply the southward depth integrated velocity, while for the Brazil and Agulhas currents the flow is the depth integrated component of velocity in the south westward direction.

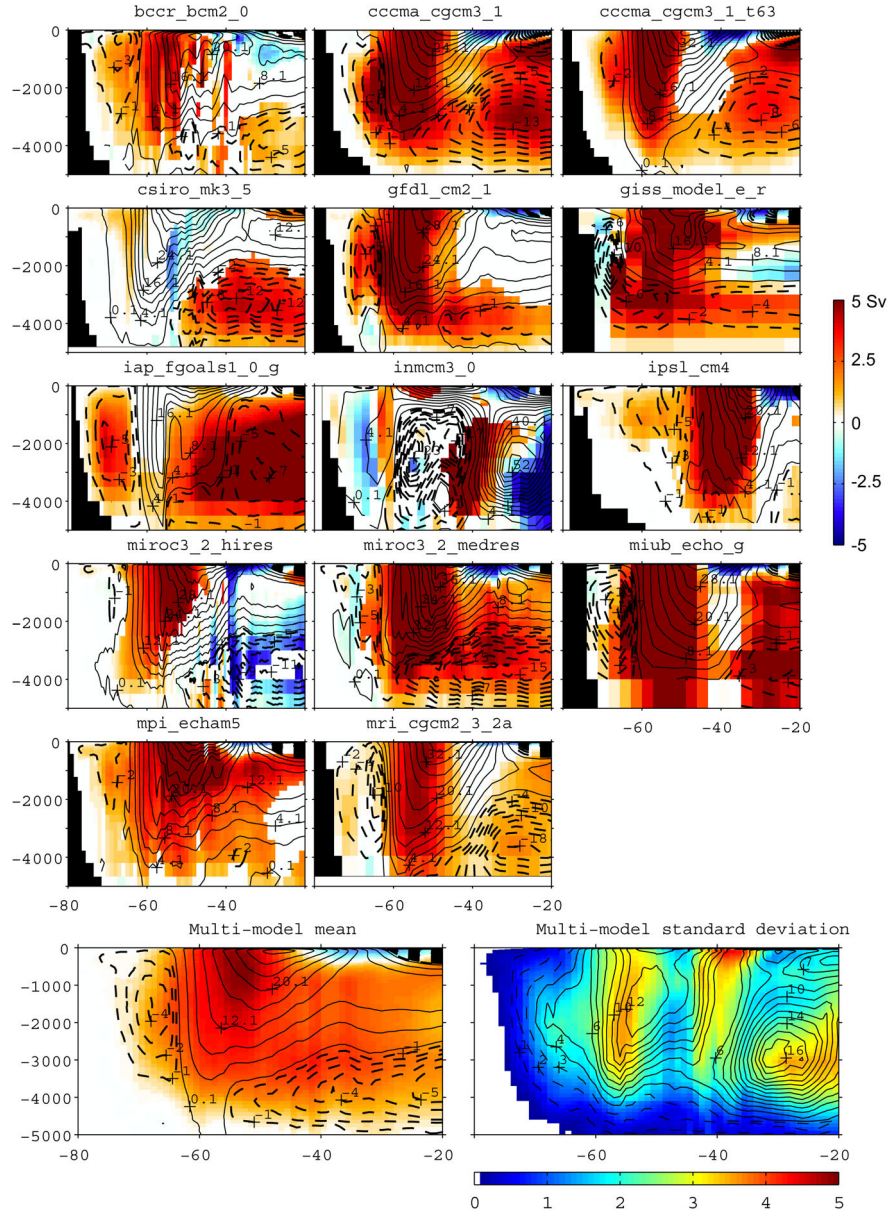


**Figure 12.** Projected change in MOC ( $21C-21C$ , colour maps). Only differences that are significant above the 95% level are displayed. The significance level is determined by two tailed t-test. The  $20C$  mean state of MOC is superimposed. Bottom left panel shows multi-model mean of  $20C$  MOC [solid contours for positive MOC (4Sv interval), dashed for negative (1Sv interval)] and projected changes (colour map). Bottom right panel shows the multi-model standard deviation for both the  $20C$  mean states (contours with 1Sv interval) and projected changes (colour map).

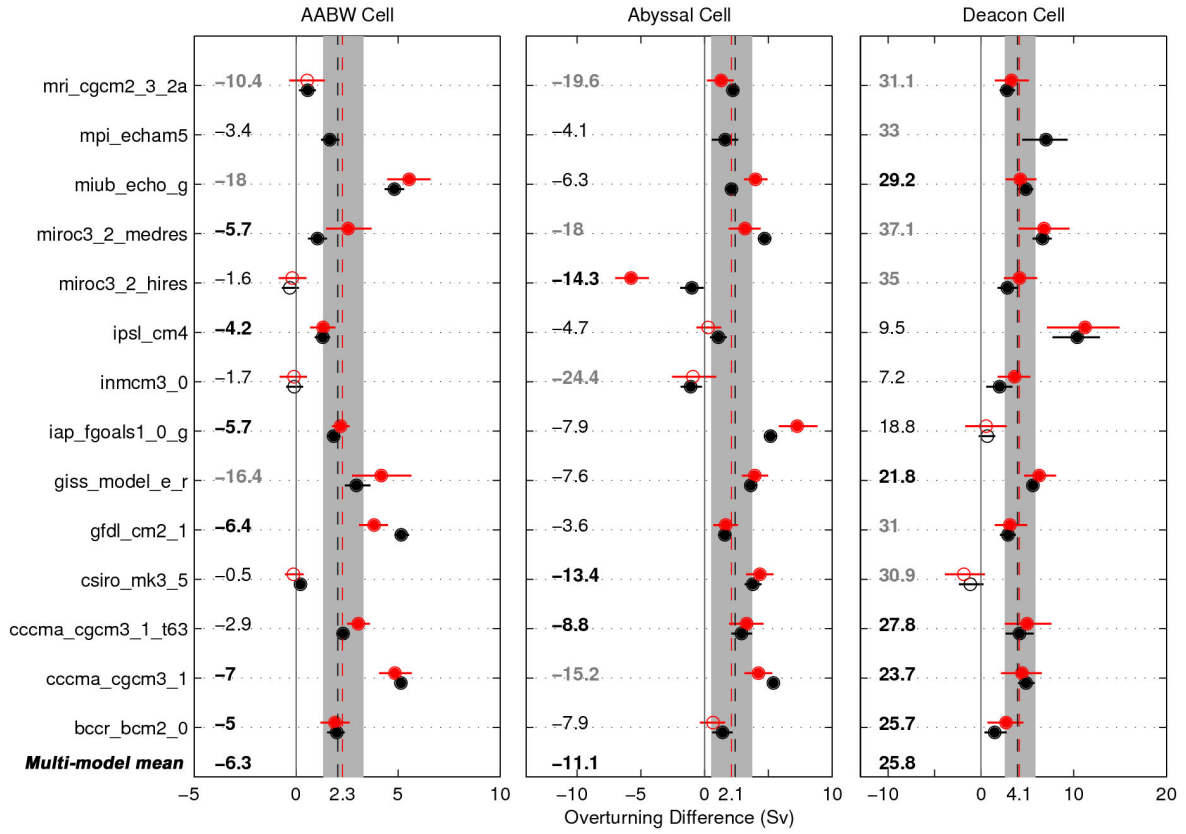


**Figure 13.** Projected differences in the transport [ $Sv$ ] of the Southern Ocean overturning cells for individual models (circles). Red circles indicate that the data have been drift corrected while black circles are based on uncorrected data. Horizontal error bars indicate the corresponding 95% confidence interval with filled circles indicating significant difference from zero. The multi-model mean differences (corrected and uncorrected) are indicated by the corresponding dashed vertical lines with the grey region indicating the 95% confidence interval for the red (drift corrected) vertical line. The 20C mean values of each model overturning cell are shown on the left of each panel with the multi-model mean values shown in bold at the bottom. Mean values that fall within 95% confidence interval of the multi-model mean are also shown in bold while the values that fall in the upper (lower) tail of the 95% interval are shown in grey (black). Note that the pre-industrial run of ECHAM5 is not available for estimating the drift. Its uncorrected values are shown nonetheless.

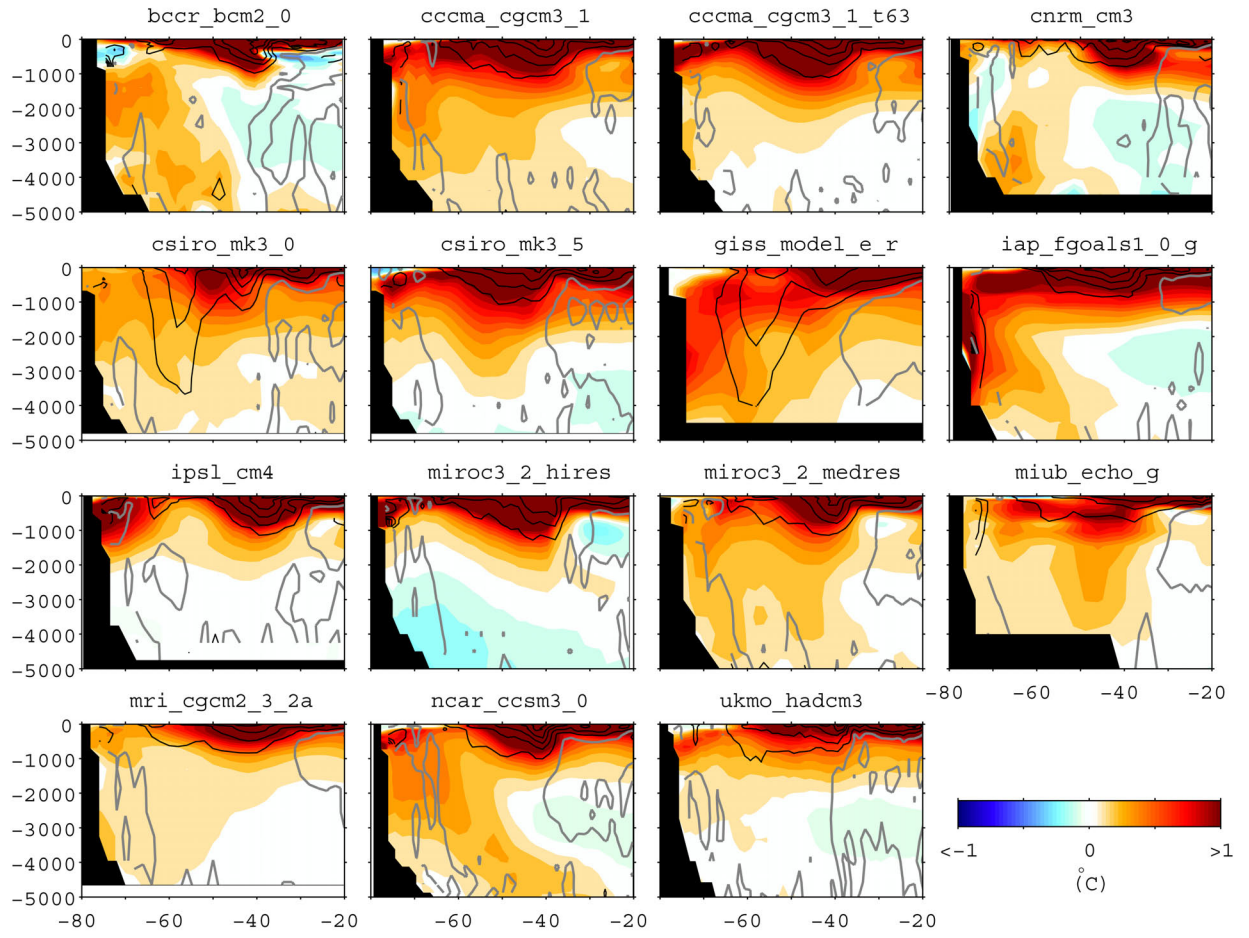


**Figure 14.** Projected change in the zonally averaged potential temperature (colour contours). Superimposed contours indicate the changes that would result from a southward shift of the  $20^{\circ}\text{C}$  temperature distribution by  $1^{\circ}$  latitude. Contour interval  $0.2^{\circ}\text{C}$ , with zero contour in grey. Black solid (dashed) contours indicate positive (negative) changes with an absolute maximum value of  $1^{\circ}\text{C}$ .



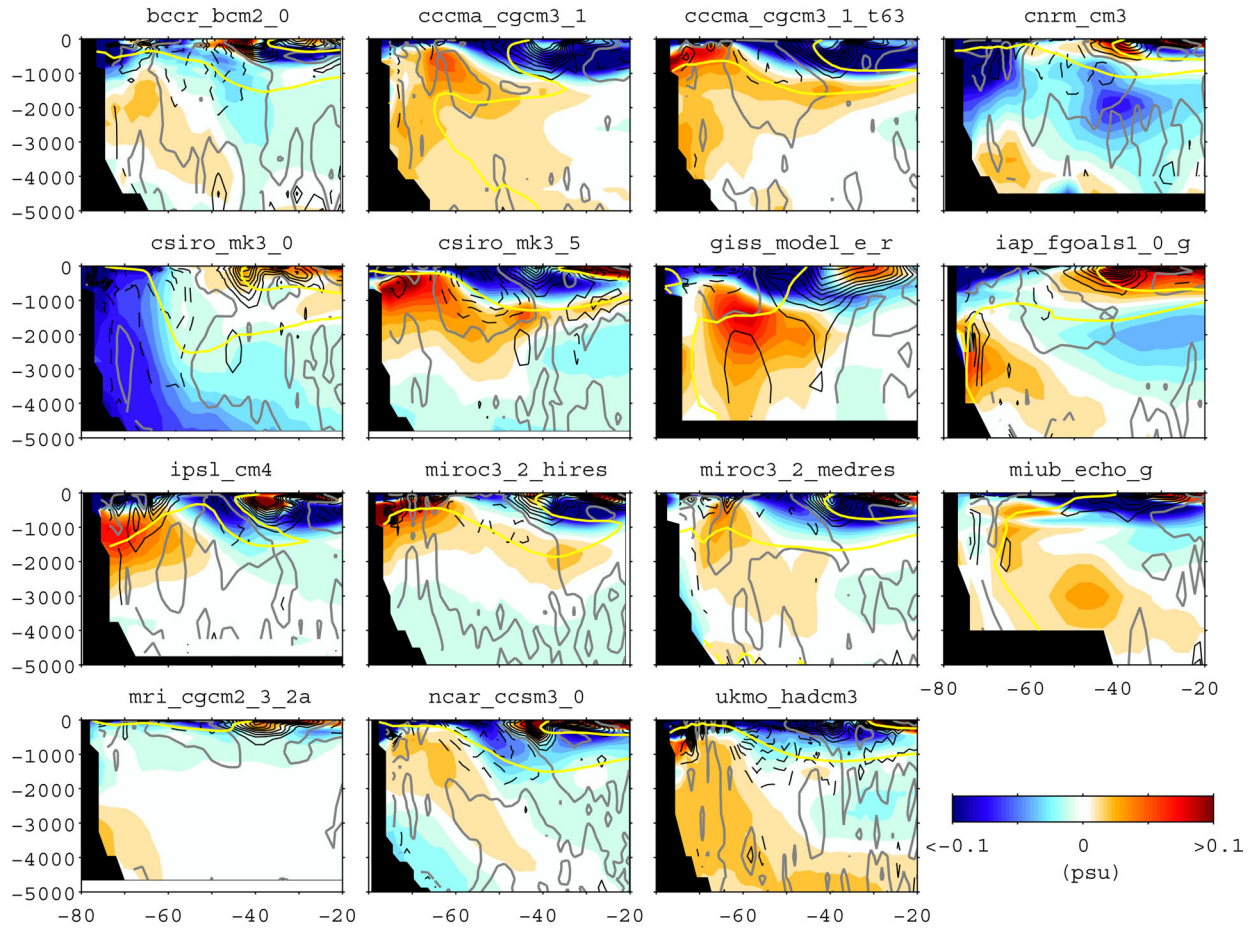


**Figure 15.** As Fig. 14 for salinity. Yellow contour is a salinity contour representative of the salinity minimum, associated with the pathway of intermediate water. Line contour interval is 0.01 psu with an absolute maximum contour value of 0.1 psu

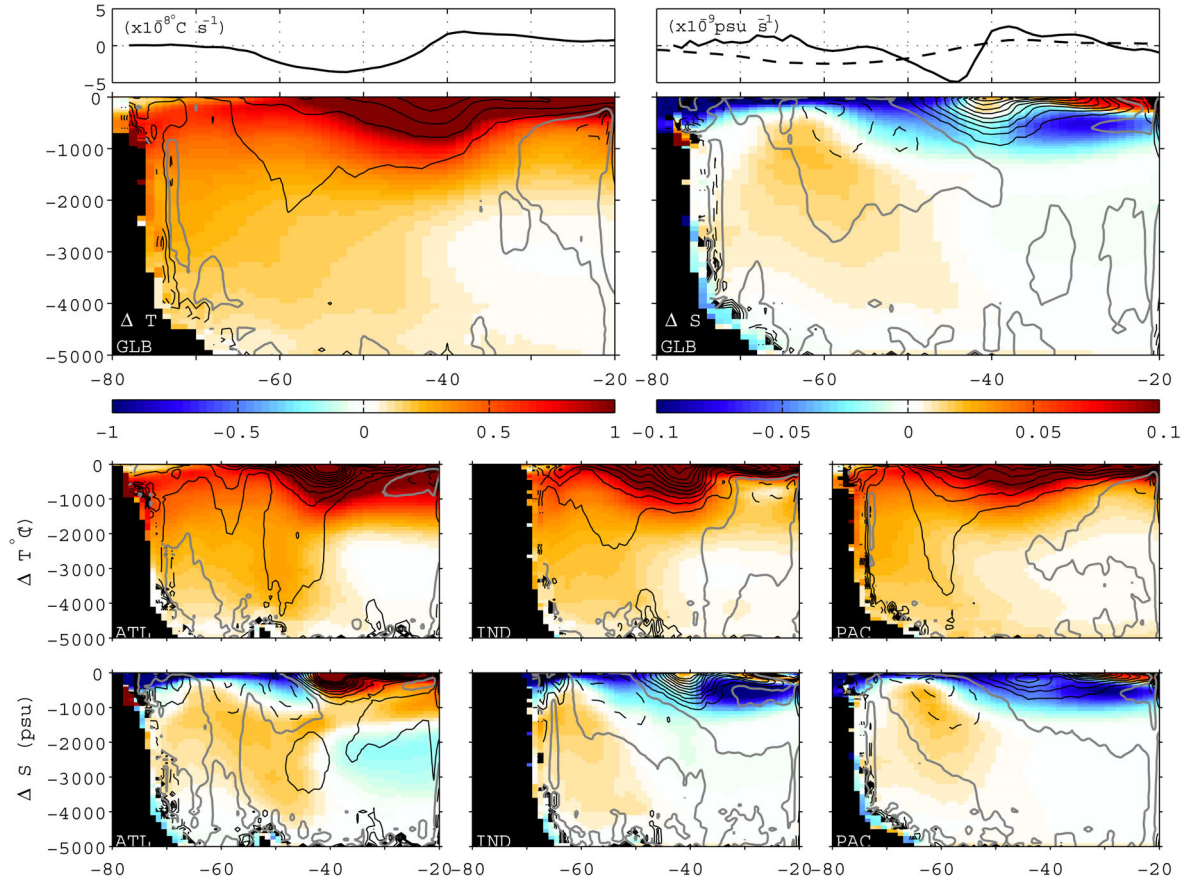


**Figure 16.** As for figs. 14 and 15 for multi-model mean global and individual basin zonal averages. Upper panels show the anomalous (*21C-20C*) Ekman related transport of heat (left) and salt (right). Right panel also shows the anomalous salt flux due to precipitation (dashed curve), using a 50m surface layer.

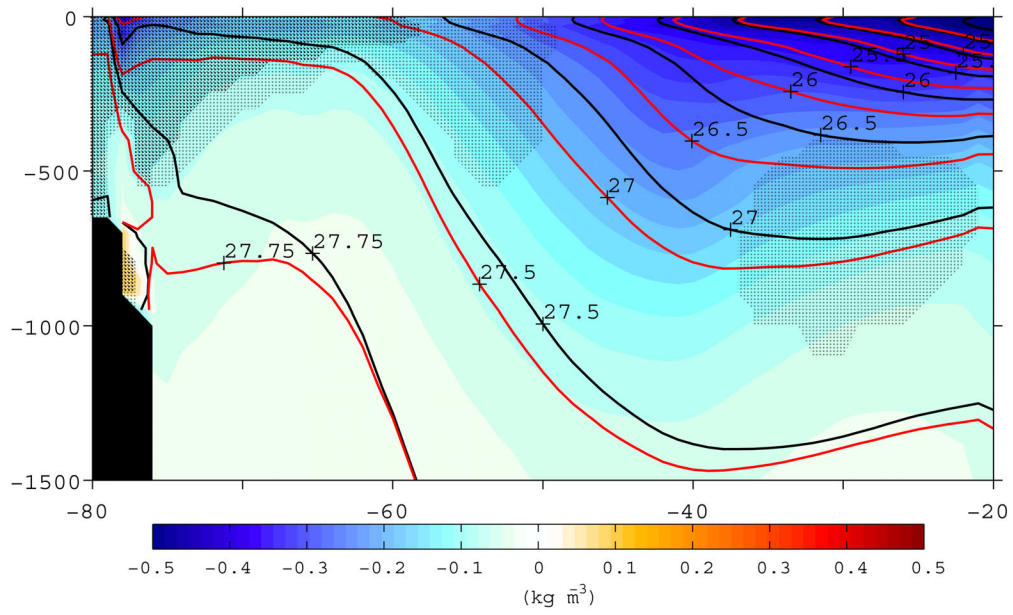


**Figure 17.** Projected change in potential density over the 21st century (colour contours). Superimposed are *20C* (black) and *21C* (red) isopycnals. Mottling indicates regions where salinity is playing a large role (>50% heavy mottling, >25% light mottling) in controlling the density change.



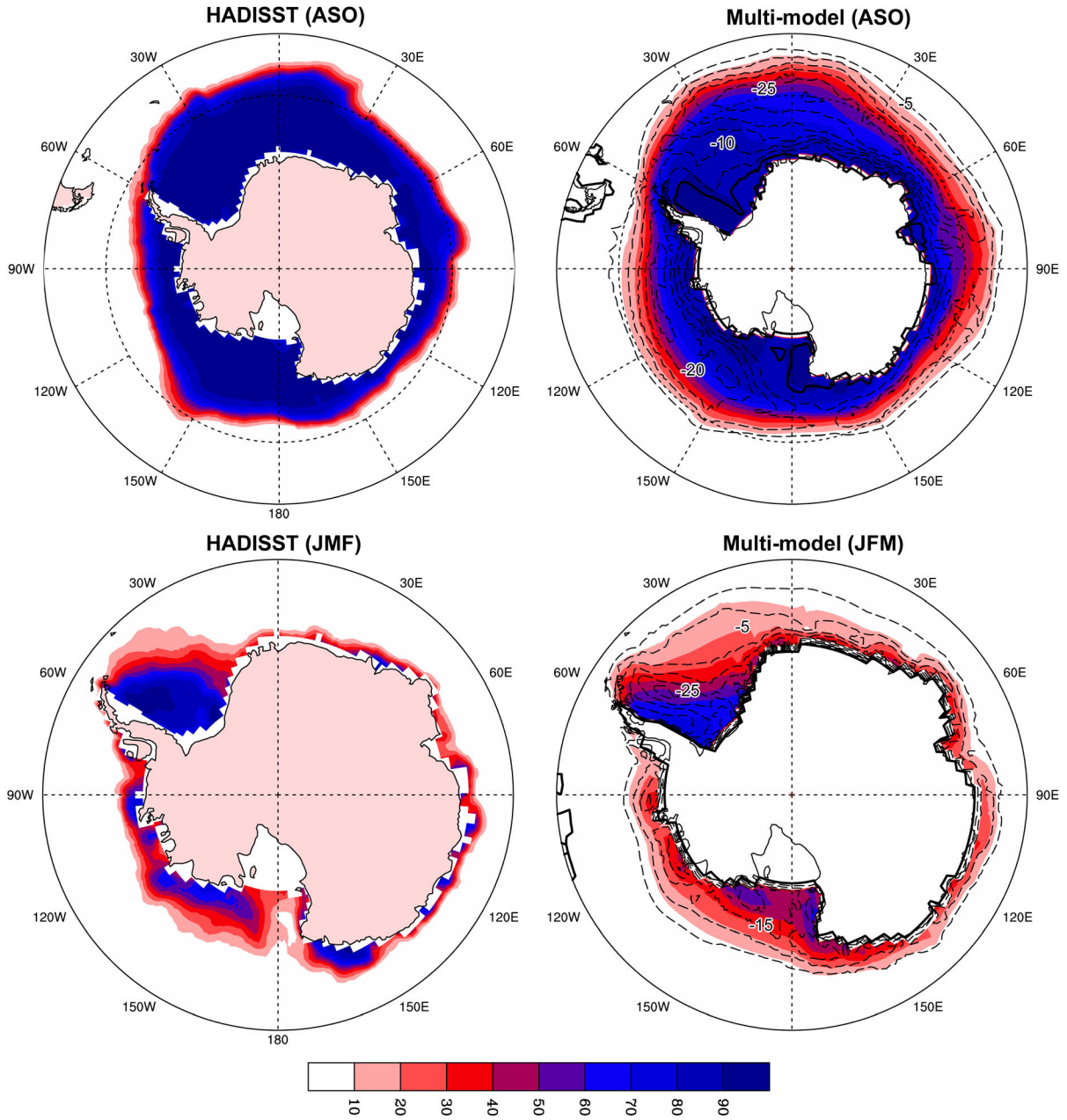


**Figure 18.** Winter (top) and summer (bottom) 20C sea-ice concentration (% cover) for observation (left) and multi-model mean (right; excluding *FGOALS-g1.0*). Superimposed contours show the percentage change in sea-ice concentration between 20C and 21C (contour interval 5%, dashed contours denote reduction in sea-ice).

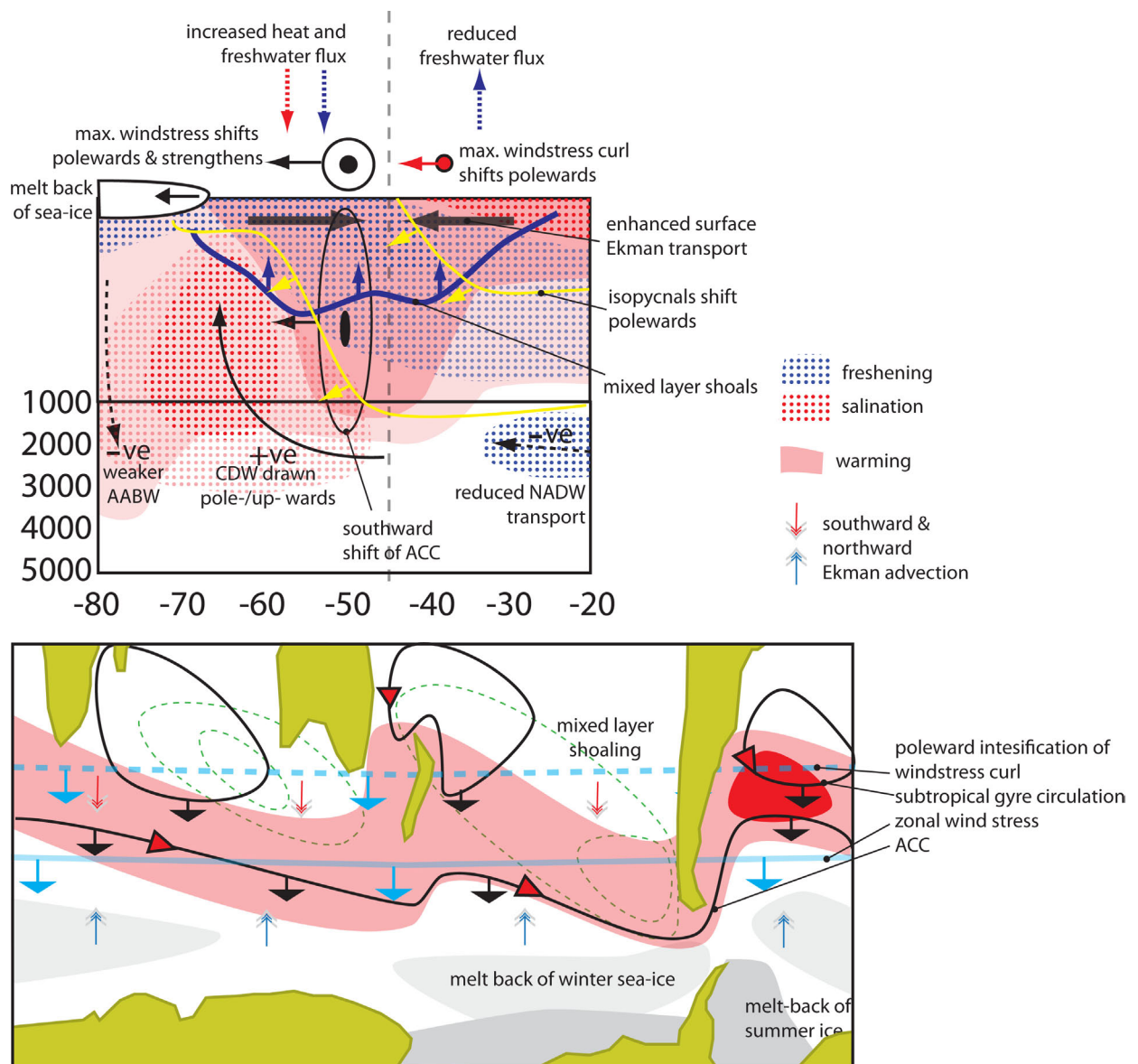


**Figure 19.** Schematic showing the robust changes in the SH extratropics.

**Table 1.** AR4 models details. Vertical coordinate: Z -depth, P -pressure, M -mass per unit area, E -topography-weighted, RHO -isopycnal, S -sigma, H -hybrid. Parametrization: GM -Gent and McWilliams (1990); GM\* - Griffies (1998) implementation of GM; BL -Bryan and Lewis (1979) depth varying vertical mixing; PP -Vertical eddy viscosity and diffusion (Pacanowski and Philander, 1981); NK -Noh and Kim (1999) Vertical diffusion and viscosity; EVD -convective mixing parametrisation; TKE -(Blanke and Delecluse, 1993); V -Visbeck *et al.* (1997) controls eddy-induced transport coefficient; KT -Kraus-Turner, wind-generated turbulent kinetic energy; KPP -mixed-layer scheme (Large *et al.*, 1994). Bottom boundary layer (BBL) -BBL-NS (Nakano and Sugimotohara, 2002); BBL-BD -(Beckmann and Döscher, 1997); NO-BBL. Flux correction: N - none; H - heat; F - freshwater; M - momentum. Forcing (anthropogenic): ALL (greenhouse gasses, ozone, and sulfate aerosols); -O: no anthropogenic ozone. Further details and references are available at PCMDI website (<http://www.pcmdi.llnl.gov/>)

Model	Oceanic Model	Oceanic Resolution	Vertical Coordinate	Mixing Parameterization	Ice Dynamic, rheology	Atmospheric Resolution	Flux Correction	Forcing	Reference
BCCR BCM2.0	MICOM2.8	1.5°x1.5°(0.5°) L35	RHO	KT, KPP	H	T63 L31	N	ALL -O	Furevik et al (2003)
CGCM3 T47	MOM1.1	1.85°x1.85° L29	Z	GM, EVD	FH, H, S	T47 L31	HF	-	Kim et al (2002)
CGCM3 T63	MOM1.1	1.41° x 0.94° L29	Z	GM, EVD	FH, H, S	T63 L31	HF	-	
CNRM CM3	OPA8.1	2°(0.5°)x2° L31	Z	GM, TKE	HD	T63 L45	N	ALL -O	Salas-Méila et al (2005)
CSIRO Mk3.0	MOM2.2	0.84°x1.875° L31	Z	GM*, BL, PP	S, FH, OF	T63 L18	N	-	Gordon et al (2002)
CSIRO Mk3.5	MOM2.2	0.84°x1.875° L31	Z	GM*, BL, PP, V, KT	S, FH, OF	T63 L18	N	-	
GFDL CM2.0	OM3P4	1°(1/3°) x1° L50	Z	GM*, BL, BBL-BD, KPP	S*, HD	2.5°x2° L24	N	ALL	Delworth et al (2006)
GFDL CM2.1	OM3.1P4	1°(1/3°) x1° L50	Z	GM*, BL, BBL-BD, KPP	S*,HD	2.5°x2° L24	N	ALL	
GISS-ER	Russell et al (1995; 2000)	4°x5° L13	Z-M	GM*, KPP	Russell et al (1995)	4°x5° L9	N	ALL	Schmidt et al (2005)
IAP FGOALS	LICOM1.0	1°x1° L33	E	GM, PP	S	T42 L26	N	ALL	Yu et al (2004)
INGV ECHAM4	OPA8.2	2°x2°(1°) L31	Z	BBL-BD, TKE	H	T106 L19	N	ALL -O	Valecke et al. (2000)
INM CM3.0	INMCM3	2°x2.5° L33	S	PP	Yakovlev (2003)	4°x5° L21	F	ALL	Diansky and Volodin (2002)
IPSL CM4	OPA	2°x2° (1°) L31	Z	GM, BBL-BD, EVD, TKE	H	2.5°x3.75° L19	N	ALL -O	Marti et al. (2005)
MIROC Hires	COCO3.3	0.19°x0.28° L47	H	GM, NK, BBL-NS, EVD	S, H, HD	T106 (1.12°x1.12°) L56	N	ALL	K-1 model developers (2004)
MIROC Medres	COCO3.3	1.4°(0.5°) x1.4° L43	H	GM, NK, BBL-NS, EVD	S, H, HD	T42 (2.81°x2.81°) L20	N	ALL	
MIUB ECHO-G	HOPE-G	2.8°x2.8° (0.5°) L20	Z	PP, EVD	S, H	T30 (3.75°x3.75°) L19	HF	ALL	Min et al. (2005)
MPI ECHAM5	MPI-OM	1.5°x1.5° L40	Z	GM*, PP, BBL-BD	S, H	T63 (1.875°x1.875°) L31	N	ALL	Jungclaus et al (2006)
MRI CGCM2.3.2a	Bryan-Cox	2.0°(0.5°)x2.5° L23	Z	GM	Mellor and Kantha (1989)	T42 L30	HFM	ALL -O	Yukimoto et al (2001);
NCAR CCSM3	POP	1.1°(0.27°)x1.1° L40	Z	GM, KPP, NO-BBL	S, FH, HD	T85 L26	N	ALL	Collins et al. (2006)
NCAR PCM1	POP	2/3°(0.5°)x2/3° L32	Z	GM, KPP, NO-BBL	S, FH, HD	T42 L18	N	ALL	Washington et al (2000)
UKMet HadCM3	Bryan-Cox	1.25°x1.25° L20	Z	GM*, V, KT, PP	H, S	2.75°x3.75°L19	N	ALL	Gordon et al (2000); Johns et al. (2003)
UKMet HadGem1	Bryan-Cox	1°(1/3°) x1° L40	Z	GM*, V, KT, PP	H, HD, S	1.25°x1.875° L38	N	ALL	Johns et al. (2006)

**Table 2.** Position of the maximum zonal wind stress for  $20C$ , zonally averaged over the Southern Ocean (Total) and over each ocean basin and the associated projected differences between  $21C$  and  $20C$ . Bold numbers, for individual models, indicate an equatorward displacement of the maximum wind stress position.

Zonal Wind Stress Position	ZONAL WIND STRESS POSITION							
	Total		Atlantic Sector 50W-20E		Indian Sector 30E-100E		Pacific Sector 180E-90W	
	20C3M ( $^{\circ}$ S)	A1B 2 - 20C3M ( $^{\circ}$ S)	20C3M ( $^{\circ}$ S)	A1B 2 - 20C3M ( $^{\circ}$ S)	20C3M ( $^{\circ}$ S)	A1B 2 - 20C3M ( $^{\circ}$ S)	20C3M ( $^{\circ}$ S)	A1B 2 -20C3M ( $^{\circ}$ S)
<b>Observation (ERA)</b>	<b>-53.2</b>	<b>-</b>	<b>-50.0</b>	<b>-</b>	<b>-49.9</b>	<b>-</b>	<b>-57.5</b>	<b>-</b>
<b>Multi-model mean</b>	<b>-49.3</b>	<b>-1.2</b>	<b>-48.6</b>	<b>-1.2</b>	<b>-48.2</b>	<b>-0.8</b>	<b>-50.5</b>	<b>-1.7</b>
<i>CGCM3.1(T47)</i>	-48.0	-2.4	-47.7	-1.7	-48.3	-1.3	-48.3	-3.8
<i>CGCM3.1(T63)</i>	-50.5	-2.1	-49.2	-1.7	-49.5	-1.4	-52.2	-3.1
<i>CNRM-CM3</i>	-46.7	-0.7	-46.1	-0.9	-45.8	-1.1	-47.7	-0.7
<i>CSIRO3.0</i>	-51.0	-0.7	-49.7	-1.2	-50.4	-0.6	-53.5	-0.8
<i>CSIRO3.5</i>	-53.7	-0.5	-52.0	-1.5	-51.5	-0.6	-57.7	<b>0.0</b>
<i>GFDL-CM2.0</i>	-47.3	-1.5	-47.	-1.2	-47.2	-0.6	-47.7	-2.6
<i>GFDL-CM2.1</i>	-52.1	-0.9	-50.1	-1.1	-50.0	-0.7	-54.9	-1.1
<i>GISS-AOM</i>	-43.5	-0.8	-44.2	-0.6	-43.8	-0.4	-42.1	-1.5
<i>FGOALS-g1.0</i>	-49.6	<b>0.1</b>	-48.3	0	-48.5	<b>0.3</b>	-51.1	<b>0.1</b>
<i>ECHAM4</i>	-54.4	-0.8	-52.2	-1.0	-51.0	-0.6	-57.5	-0.8
<i>INM-CM3.0</i>	-49.0	-0.5	-49.4	-0.2	-47.3	-0.4	-49.8	-0.7
<i>IPSL-CM4</i>	-42.4	-3.1	-44.3	-2.3	-42.6	-2.4	-40.1	-5.2
<i>MIROC3.2(hires)</i>	-49	-1.1	-48.1	-0.9	-48.3	-0.5	-49.8	-1.7
<i>MIROC3.2(medres)</i>	-46.9	-1.8	-46.9	-1.5	-46.6	-1.0	-46.8	-2.8
<i>ECHO-G</i>	-47.2	-4.2	-47.3	-3.1	-46.9	-2.7	-48.2	-5.7
<i>ECHAM5</i>	-50.3	-0.8	-49.4	-1.1	-49.0	-0.9	-52.6	-0.6
<i>MRI-CGCM2.3.2</i>	-50.5	-0.7	-49.5	-1.0	-49.7	-0.6	-52.2	<b>0.2</b>
<i>CCSM3</i>	-52.1	-1.0	-50.7	-1.2	-49.8	-0.9	-54.7	-1.3
<i>PCM</i>	-51.4	<b>0.2</b>	-50.8	<b>0.1</b>	-50.0	<b>0.08</b>	-53.9	<b>0.5</b>

**Table 3.** ACC transport calculated as the difference in the stream function across the Drake Passage. (\*)Where stream function data is unavailable it has sometimes been possible to estimate transport using the zonal velocity integrated across the passage through the water column (different model groups have made available different variable sets).

	<i>20C (sv)</i>	<i>21C (sv)</i>	Difference
<i>BCCR BCM2.0*</i>	95.9	92.4	-3.7
<i>CGCM3.1(T47)</i>	97.4	100.3	3.0
<i>CGCM3.1(T63)</i>	110.2	121.9	10.6
<i>CNRM-CM3</i>	83.8	58.7	-29.9
<i>CSIRO3.0</i>	312.8	296.9	-5.1
<i>CSIRO3.5</i>	148.9	156.8	5.3
<i>GISS-ER</i>	226.1	223.4	-1.2
<i>FGOALS-g1.0</i>	71.0	65.6	-7.5
<i>ECHAM4*</i>	139.0	131.0	-5.8
<i>INM-CM3.0</i>	72.1	91.8	27.4
<i>IPSL-CM4</i>	44.2	50.5	14.2
<i>MIROC3.2(hires)</i>	121.6	134.0	10.2
<i>MIROC3.2(medres)</i>	185.1	183.7	-0.8
<i>ECHO-G</i>	71.4	73.3	2.8
<i>ECHAM5</i>	154.8	161.4	4.3
<i>MRI-CGCM2.3.2</i>	93.5	95.5	2.1
<i>CCSM3*</i>	205.4	190.2	-7.4
<i>PCM *</i>	250.3	241.3	-3.6
<i>HadCM3</i>	216.0	218.8	1.3
<b><i>Multi-model mean</i></b>	<b>144.6</b>	<b>144.2</b>	
<b><i>Observation</i></b>	<b>135</b>		

**Table 4.** Total Antarctic sea-ice area ( $\times 10^{14} m^2$ ) and volume ( $\times 10^{14} m^3$ ) for summer (JFM) and winter (ASO) seasons for *20C* and *21C* periods. Last column shows the percentage change over the 21<sup>st</sup> century in the ASO to JFM difference in ice volume (i.e. a measure of the change in the seasonal cycle).

	SIC				Ice Volume				% change
	Winter		Summer		Winter		Summer		
	20C	21C	20C	21C	20C	21C	20C	21C	
<i>BCCR BCM2.0</i>	13.3	7.7	2.1	0.6	13.3	5.3	2.1	0.4	-57
<i>CGCM3.1(T47)</i>	20.0	18.0	4.9	3.0	12.5	12.0	3.2	2.1	6
<i>CGCM3.1(T63)</i>	24.4	18.4	7.0	2.5	13.8	10.7	4.2	1.2	-1
<i>CNRM-CM3</i>	16.4	9.1	0.2	0.1	5.9	2.7	0.1	0.0	-55
<i>CSIRO3.0</i>	15.5	13.5	3.5	2.3	13.8	10.4	2.5	1.3	-19
<i>CSIRO3.5</i>	15.6	10.7	5.5	3.2	14.1	8.9	2.8	1.4	-33
<i>GISS-ER</i>	11.8	9.2	1.2	0.7	10.7	7.7	1.5	0.8	-24
<i>FGOALS-g1.0</i>	37.9	33.7	34.4	30.9	39.3	33.2	21.8	15.2	3
<i>ECHAM4</i>	12.4	9.3	1.8	1.0	8.0	5.7	1.6	1.1	-28
<i>INM-CM3.0</i>	18.0	13.3	4.0	1.8	20.0	9.3	9.6	1.9	-29
<i>IPSL-CM4</i>	14.7	10.0	0.9	0.2	10.0	5.3	1.6	0.4	-42
<i>MIROC3.2(hires)</i>	14.8	8.1	0.9	0.0	12.7	5.5	0.6	0.0	-54
<i>MIROC3.2(medres)</i>	11.2	8.8	0.8	0.4	5.8	4.1	0.5	0.1	-25
<i>ECHO-G</i>	14.2	12.9	1.0	0.6	5.0	4.2	0.4	0.2	-13
<i>ECHAM5</i>	13.2	8.3	2.6	1.0	9.1	4.9	2.2	0.6	-37
<i>MRI-CGCM2.3.2</i>	18.5	17.3	4.3	1.9	11.8	9.0	2.0	0.5	-12
<i>CCSM3</i>	19.6	16.5	5.1	1.6	23.7	18.2	7.8	2.1	1
<i>PCM</i>	14.3	10.7	3.7	2.7	11.2	7.3	3.9	2.3	-31
<i>HadCM3</i>	11.2	13.8	2.5	1.5		15.6	4.0	1.5	
<i>HadGem1</i>	18.5	14.3	4.1	2.3	24.3	18.5	11.1	8.6	-25
<i>Multi-model mean</i>	<b>15.7</b>	<b>12.1</b>	<b>3.0</b>	<b>1.4</b>	<b>12.5</b>	<b>8.7</b>	<b>3.2</b>	<b>1.4</b>	<b>-27</b>
<i>HadISST (obs)</i>	<b>16.0</b>		<b>3.1</b>						